J. Fluid Mech. (1996), *vol.* 317, *pp.* 301–335

Subharmonic transition to turbulence in a flat-plate boundary layer at Mach number 4.5

By N. A. ADAMS † AND L. KLEISER †

DLR, Institute of Fluid Mechanics, Bunsenstraße 10, D-37073 Göttingen, Germany

(Received 27 August 1993 and in revised form 16 November 1995)

The subharmonic transition process of a flat-plate boundary layer at a free-stream Mach number of $M_\infty = 4.5$ and a Reynolds number of 10000 based on free-stream velocity and initial displacement thickness is investigated by direct numerical simulation up to the beginning of turbulence. A second-mode instability superimposed with random noise of low amplitude is forced initially. The secondary subharmonic instability evolves from the noise in accordance with theory and leads to a staggered Λ-vortex pattern. Finite-amplitude Λ-vortices initiate the build-up of detached high-shear layers below and above the critical layer. The detached shear-layer generation and break-up are confined to the relative-subsonic part of the boundary layer. The breakdown to turbulence can be separated into two phases, the first being the break-up of the lower shear layer and the second being the break-up of the upper shear layer. Four levels of subsequent roll-up of the lower, Y-shaped shear layer have been observed, leading to new vortical structures which are unknown from transition at low Mach numbers. The upper shear layer behaviour is similar to that of the well-known high-shear layer in incompressible boundary-layer transition. It is concluded that, as in incompressible flow, turbulence is generated via a cascade of vortices and detached shear layers with successively smaller scales. The different phases of shear-layer break-up are also reflected in the evolution of averaged quantities. A strong decrease of the shape factor, as well as an increase of the skin friction coefficient, and a gradual loss of spanwise symmetry indicate the final breakdown to turbulence, where the mean velocity and temperature profiles approach those measured in fully turbulent flow.

1. Introduction

For incompressible flows detailed experiments, theoretical efforts and numerical simulations have led to a basic understanding of the boundary-layer transition process. In a low-disturbance environment the initial stages can essentially be treated by linearized theories (Mack 1984; Herbert 1988). At higher Mach numbers the linear stability characteristics become substantially more complex compared to incompressible flow (Mack 1984, 1990; Ng & Erlebacher 1992). One observes that the most unstable linear eigenmodes at low supersonic Mach numbers are oblique vortical modes. These give rise to a particular transition mechanism, called the oblique-mode breakdown, where nonlinear interactions take over without a secondary instability

† Present address: Institute of Fluid Dynamics, ETH Zentrum, CH-8092 Zürich, Switzerland.

mechanism following the primary one. It was first identified by numerical simulations of Thumm, Wolz & Fasel 1990, and the late stages of breakdown have been investigated by Sandham, Adams & Kleiser (1994). Experimental evidence for the dominance of oblique linear eigenmodes at low supersonic Mach numbers has been given by Kosinov, Maslow & Shevelkov (1990). At Mach numbers beyond a threshold of about $M_\infty = 3$ a two-dimensional second mode or Mack mode (Mack 1984), which is of mixed vortical–acoustic type and moves with a low subsonic velocity relative to the freestream, becomes most unstable. Experimental evidence for the existence of this mode was first given by Kendall (1967), though its significance in initiating laminar turbulent breakdown is controversial. Experimental results by Stetson & Kimmel (1992) do not seem to indicate that the transition, even at high Mach numbers ($\geqslant 6.8$), is initiated by a subharmonic mechanism which is supposed to follow a dominant two-dimensional second-mode instability. Simulations by Guo, Kleiser & Adams (1996), however, show that in a favourable environment subharmonic transition at high supersonic Mach numbers ($\simeq 4.5$) is not precluded. Other possible scenarios at this Mach number range are the oblique mode breakdown following a first eigenmode (Adams & Kleiser 1993*b*) or a breakdown following an oblique second eigenmode as suggested by Stetson & Kimmel (1992) and recently investigated numerically by Pruett & Chang (1995).

Owing to the enormous difficulties of controlled experiments for high-supersonic flows hardly any experimental results revealing detailed flow phenomena at the nonlinear stages of supersonic transition have been published. Instead, they have been mostly restricted to the domain of linear disturbance growth. A considerable amount of data for different configurations is available for fully turbulent flow (for a compilation see e.g. Fernholz & Finley 1977). Often, however, experiments even qualitatively disagree with respect to correlations such as RMS (root-mean-square) profiles of velocity and temperature fluctuations or Reynolds stresses. Specific correlations appearing in the compressible turbulence closure problem such as the pressure–dilatation correlation or the compressible dissipation (Sarkar *et al.* 1991; Zeman 1990) may not be obtainable by present experimental techniques. Assumptions about the effect of compressibility presently used in the modelling of compressibility effects in turbulent flows are mainly extrapolations from isotropic decaying and homogeneous shear turbulence which still need to be verified or qualified for inhomogeneous flows.

Only a few experimental investigations have considered the evolution of organized structures in turbulent compressible boundary layers. Spina & Smits (1987), using conditional sampling and correlations of mass flux and pressure, found structures in a turbulent boundary layer at a Mach number of 3 which extend to about 30% of the boundary-layer thickness and possess small spanwise but large streamwise scales. The inclination of these structures changes from about 15° near the wall to about 45° in the mid-region of the boundary-layer and up to about 70° to 90° in the outer region. Similar results have been obtained by Owen & Horstman (1972) for a turbulent boundary layer at Mach 7.2. No similar experimental studies are known for transitional high-speed boundary layers. Using direct numerical simulation data Sandham & Kleiser (1992) identified a mechanism for generation of near-wall turbulence for incompressible channel flow. Its basic ingredients are streamwise vortices and detached shear layers which are generated in a chain-like manner with successively smaller scales until the viscous limit is reached. One open question, to be addressed in the present paper, has been whether a similar mechanism is valid at high Mach number.

Owing to this lack of experimental data there is a strong interest in numerical

simulation techniques for studying transition. Both temporal (Erlebacher & Hussaini 1990; Adams, Sandham & Kleiser 1992, Pruett & Zang 1992; Adams & Kleiser 1993*a, b*) and spatial (Thumm *et al.* 1990, Fasel, Thumm & Bestek 1993; Pruett & Chang 1993, 1995; Eißler & Bestek 1993; Pruett *et al.* 1995) simulation models have been successfully applied to moderate and high Mach number flows. Pruett & Zang (1992) investigated the subharmonic transition of a boundary layer on a hollow cylinder at flow parameters close to those of the present study.

The closest realization of a transition experiment by numerical simulation is the so-called spatial model. In this model, the Navier–Stokes equations are solved subject to suitable inflow and outflow boundary conditions and no *a–priori* assumptions about the mean flow are necessary. If a perturbation is forced in accordance with an experiment the instability evolves equivalently. In particular, mean-flow non-parallelity is accounted for. Following the regime of linear and weakly nonlinear interactions, strongly nonlinear interactions take place at the late stages of transition, within a short streamwise region. During this stage non-parallel effects of the mean flow can be neglected. This particular stage of transition immediately before the onset of turbulence is investigated in the present paper. It cannot be studied by other means than experiments or direct numerical simulations owing to the strong interaction between mean flow and perturbations. A temporal simulation method comprises a region just long enough to represent all significant mode interactions. Instead of imposing inflow and outflow boundary conditions, the flow is assumed to be streamwise periodic with a certain fundamental wavelength. The corresponding instability is temporal (Mack 1984) and the flow evolves in time instead of space. In a temporal simulation as used here, the fundamental instability mechanism needs to be selected *a priori*. Note, however, that a significant improvement in matching a temporal model to a spatial instability can be obtained by including mean-flow non-parallelity effects to a certain degree (Guo *et al.* 1996; Guo, Adams & Kleiser 1995).

In the present paper we investigate the late stages of transition in a flat-plate boundary layer following a subharmonic instability at a free-stream Mach number of $M_\infty = 4.5$ and a Reynolds number of 10000 based on the initial displacement thickness. The subharmonic transition mechanism is well known in incompressible flow (Herbert 1988). For high Mach number boundary layer the existence of a subharmonic secondary instability following a two-dimensional second mode has been shown by Ng & Erlebacher (1992). It is stressed that the subharmonic transition following a second mode is a genuine compressible phenomenon and so is the following breakdown. In contrast to fully developed turbulence, which is statistically independent of its transition history, compressibility cannot be expressed in terms of isolated or parameterizable events. In this paper emphasis is placed on documentation and analysis of physical phenomena during transition in terms of the evolution of organized structures. The basis of the investigation are numerical data obtained by a temporal direct simulation. A concise description of the numerical simulation method is given in §2. The simulation results are presented in §3. In §4 the findings are discussed and conclusions are given in §5.

2. Simulation method

2.1. *Mathematical model*

The problem considered is that of transition to turbulence in the boundary layer along a flat plate. The temporal simulation approach is adopted, allowing the use

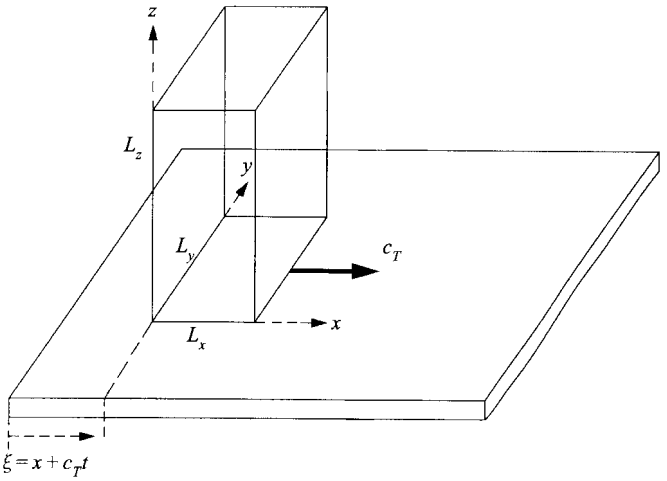

FIGURE 1. Sketch of the computational domain.

of periodic boundary conditions in the streamwise and spanwise directions x and y. The integration domain has the extents L_x in the streamwise and L_y in the spanwise direction and is truncated at L_z in the wall-normal direction. A sketch of the integration domain is shown in figure 1, together with the Cartesian coordinate system $\{x, y, z\}$. For ease of notation in the following an index notation (with summation convention) is used, where the subscripts 1, 2 and 3 correspond to the coordinates x, y and z, respectively.

The basic equations to be solved are the three-dimensional unsteady compressible Navier–Stokes equations in conservation form. The basic flow is imposed by the standard technique of adding a forcing term (see below), which in the present simulation is kept constant in time as the simulation is done in a frame of rest. A perfect gas with specific heat ratio $\kappa = 1.4$ is assumed. In the following, dimensional quantities are marked by an asterisk. The non-dimensionalization is done by

$$u_i = u_i^*/U_\infty^*\,, \quad \rho = \rho^*/\rho_\infty^*\,, \quad T = T^*/T_\infty^*\,, \quad p = p^*/(\rho_\infty^* U_\infty^{*2})\,, \quad E_T = E_T^*/(\rho_\infty^* U_\infty^{*2}).$$

Here u_i denotes the velocity components, ρ the density, p the pressure and E_T the total energy to be defined below. The time t is non-dimensionalized by U_∞^*/δ_1^*, where the reference length δ_1^* is taken as the displacement thickness of the undisturbed laminar basic flow. The governing equations can be cast in non-dimensional form as (e.g. Adams 1993)

$$\frac{\partial \rho}{\partial t} = -\frac{\partial \rho u_i}{\partial x_i} + Z_1, \tag{2.1}$$

$$\frac{\partial (\rho u_i)}{\partial t} = -\frac{\partial (\rho u_i u_j + p\delta_{ij})}{\partial x_j} + \frac{\partial \tau_{ij}}{\partial x_j} + Z_{i+1}, \tag{2.2}$$

$$\frac{\partial E_T}{\partial t} = -\frac{\partial (E_T + p) u_i}{\partial x_i} - \frac{\partial q_i}{\partial x_i} + \frac{\partial (u_j \tau_{ij})}{\partial x_i} + Z_5\,, \tag{2.3}$$

with the total energy $E_T = p/(\kappa - 1) + u_i u_i/2$ and for $i, j = 1, 2, 3$. The shear-stress tensor obeying Newton's relation and Stokes' hypothesis is given by

$$\tau_{ij} = \frac{\mu}{Re}\left(\frac{\partial u_i}{\partial x_j} + \frac{\partial u_j}{\partial x_j} - \frac{2}{3}\frac{\partial u_k}{\partial x_k}\delta_{ij}\right)\,, \tag{2.4}$$

and the heat flux vector is

$$q_i = -\frac{\mu}{(\kappa-1)M_\infty^2 PrRe}\frac{\partial T}{\partial x_i}\,. \tag{2.5}$$

The Reynolds number of the flow is defined as $Re = U_\infty^* \delta_1^* / \nu_\infty^*$, and the Prandtl number $Pr = c_p^* \mu_\infty^* / \lambda_\infty^*$, where c_p is the specific enthalpy and λ is the heat conductivity. The Prandtl number is set to $Pr = 0.7$. The dynamic viscosity μ is an explicit function of the temperature only and is assumed to obey Sutherland's law

$$\mu(T) = T^{3/2}\frac{1+S}{T+S}\,, \tag{2.6}$$

where $S = 110.4K/T_\infty^*$. As an additional algebraic relation the perfect-gas relation

$$\kappa M_\infty^2 p = \rho T \tag{2.7}$$

is used. Terms Z_i in equations (2.1)–(2.3) are the components of a forcing vector, given by

$$\left.\begin{aligned}
Z_1 &= c_T\frac{\partial \mathscr{P}}{\partial \xi}, \\
Z_2 &= c_T\frac{\partial(\mathscr{P}U)}{\partial \xi} - \frac{1}{Re}\frac{\partial}{\partial z}\left(\mathscr{M}\frac{\partial U}{\partial z}\right), \\
Z_3 &= Z_4 = 0, \\
Z_5 &= c_T\frac{1}{2}\frac{\partial\left(\mathscr{P}U^2\right)}{\partial \xi} - \frac{1}{(\kappa-1)M_\infty^2 PrRe}\frac{\partial}{\partial z}\left(\mathscr{M}\frac{\partial \Theta}{\partial z}\right) - \frac{1}{Re}\frac{\partial}{\partial z}\left(\mathscr{M}U\frac{\partial U}{\partial z}\right),
\end{aligned}\right\} \tag{2.8}$$

where $\xi = x + c_T t$ is the downstream coordinate in a fixed frame of reference, while the integration domain is moving downstream with some velocity c_T (as mentioned before, we choose $c_T = 0$ in the present work). The basic flow profiles are denoted by $U(z)$ (streamwise velocity), $\Theta(z)$ (temperature), $\mathscr{P}(z)$ (density) and $\mathscr{M}(\Theta)$ (viscosity).

Some explanation for the use of a forcing term is in order. We are interested in the nonlinear evolution of perturbations in a given laminar boundary layer. Thus we need to find a mathematical model which describes the perturbation evolution while keeping the *basic* flow fixed. Note that the *mean* flow, however, is allowed to evolve due to nonlinear interactions between perturbation modes. One possibility is given by explicitly splitting the flow variables into a basic flow and a perturbation and to derive a set of differential equations for the perturbations. A more concise way has been proposed by Spalart & Yang (1987) and has been used e.g. by Erlebacher & Hussaini (1990) and others for compressible flow. In order to cancel out the residual generated when the given basic flow quantities are inserted into the Navier–Stokes equations, a source term (which may in general vary in time and space) is added to the Navier–Stokes equations. The validity of this approach may become evident from the following brief analysis. We consider for this purpose the Navier–Stokes equations for a one-dimensional flow and write them as

$$\frac{\partial \boldsymbol{U}}{\partial t} = \frac{\partial \boldsymbol{F}}{\partial x} + \boldsymbol{Z}\,, \tag{2.9}$$

where

$$\boldsymbol{F} = \begin{bmatrix} -\rho u \\ -\rho u^2 - p + \tau_{xx} \\ -u(E+p) - q_x + u\tau_{xx} \end{bmatrix}. \tag{2.10}$$

By separating zeroth- and higher-order terms $\boldsymbol{F}$ may be written as (the subscript 0 indicates basic flow quantities) $\boldsymbol{F} = \boldsymbol{F}_0 + \boldsymbol{F}'$ where

$$\boldsymbol{F}' = \begin{bmatrix} -\rho_0 u' \\ -2\rho_0 u_0 u' - 2\rho' u_0 u' - \rho' u_0^2 - \rho' u'^2 - p' + \tau'_{xx} \\ -u'(E_0 + p_0) - u_0(E' + p') - u'(E' + p') - q'_x + u'\tau_{xx}|_0 + u_0\tau'_{xx} \end{bmatrix}$$

By defining $\boldsymbol{Z} := -\partial \boldsymbol{F}_0/\partial x$ equation (2.9) becomes the full nonlinear perturbation equation for a given steady laminar basic flow $\boldsymbol{U}_0$. In the case of an unsteady basic flow due to $c_T \neq 0$, the forcing is defined by $\boldsymbol{Z} := -\partial \boldsymbol{F}_0/\partial x + c_T \partial \boldsymbol{U}_0/\partial \xi$. We are mainly interested in the nonlinear interactions of all perturbation modes. This regime extends only over a relatively short streamwise section, where it is reasonable for our purpose to let $c_T = 0$ and the boundary layer be locally parallel. Certain effects of boundary-layer growth may be considered by moving the reference frame ($c_T \neq 0$). However, contrary to incompressible flow (Spalart & Yang 1987), it turns out that (2.8) does not satisfactorily take into account the effect of boundary-layer growth with respect to the linear instability modes. This problem has been addressed in a separate study and an extended form of equation (2.8) has been proposed, which takes into account the non-parallelity of the basic flow and linear perturbations within the temporal simulation method (Guo *et al.* 1995, 1996). Note that simplified models such as nonlinear PSEs (parabolized stability equations) (e.g. Pruett & Chang 1993) are not capable of accounting for all interactions.

As initial condition, the laminar basic flow is superimposed with eigensolutions of the linear stability equations and, additionally or alternatively, random fluctuations. The basic flow is given by the compressible laminar boundary-layer similarity equations for an adiabatic wall, also employing Sutherland's viscosity law (Stewartson 1964, pp. 33–60). The similarity solution is obtained numerically by a shooting method (Adams 1993). In the simulation, periodic boundary conditions are enforced in the streamwise and the spanwise directions, and a no-slip condition is used at the wall. The wall is assumed to be isothermal with respect to the fluctuations. At the upper artificial boundary $z = L_z$ time-dependent non-reflecting boundary conditions adapted from Thompson (1987) are used. For details on initial and boundary conditions the reader is referred to Adams (1993).

2.2. *Numerical method*

The periodic streamwise and spanwise directions x and y are treated by using Fourier expansions. In these directions the pseudo-spectral Fourier-collocation approach is employed (see Canuto *et al.*, 1988). In the wall-normal direction z a compact finite-difference scheme (Lele 1992) is used, which is of sixth order at inner points and has third- to fourth order boundary closures for the first- and second-derivative operators. The (Lax- and asymptotic) stability of the scheme was proved (Adams 1993) for the linear convective and the linear diffusive limits using a normal mode and an eigenvalue analysis similar to Carpenter, Gottlieb & Abarbanel (1993). For time advancement an explicit third-order compact-storage Runge–Kutta scheme (Wray 1986) is used. An analytic mapping function between the evenly spaced computational interval $[0, 1]$ and the physical wall-normal interval $[0, z_{max}]$ is used (Adams 1993). This allows for a condensation of grid points near the wall and some plane $z_c \in [0, z_{max}]$, which

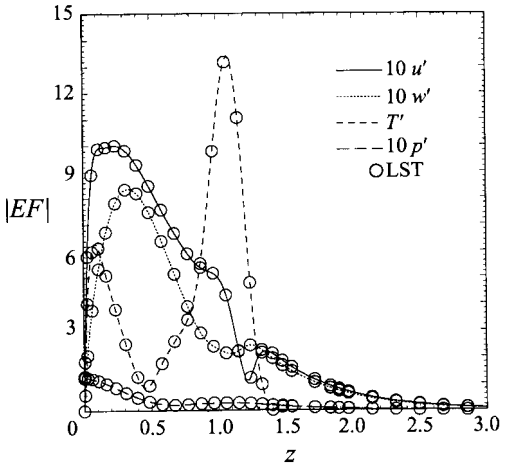

FIGURE 2. Amplitude functions: DNS solution and linear eigensolution (symbols).

is chosen to be the critical layer in our simulation. The mapping parameters are optimized for resolving linear instability waves and are kept constant throughout a simulation.

The code has been validated by computing the growth rates and shapes of linear eigenfunctions. Two classes of tests were made: (*a*) tests where eigenfunctions from linear stability analysis were used as the initial disturbances, and (*b*) tests where linear instabilities were allowed to grow from random background disturbances. In all cases very good agreement with linear theory was obtained. As an example, a comparison of the amplitude distributions of a second-mode disturbance at $M_\infty = 4.5$, $Re = 10000$ and wavenumbers $\alpha = 2.25$ (streamwise) and $\beta = 0$ (spanwise) is shown in figure 2. The initial noise level was $A = 10^{-8}$. The correct eigenfunctions were extracted from the numerical solution at $t = 305.28$. The difference between the numerical simulation results and the results from a numerical solution of the linear stability equations is less than 0.5%. The phase distributions are also in excellent agreement (Adams 1993). The solutions of the compressible linear stability equations were obtained by a spectral collocation method (Simen & Dallmann 1992). A more detailed description of the mathematical model, the numerical method, validation procedure and test results can be found in Adams *et al.* (1992) and Adams (1993).

3. Simulation results

The subject of investigation is the subharmonic route to turbulence in a $M_\infty = 4.5$ boundary layer when the secondary instability grows from background noise. Emphasis is placed on the flow-field structure at nonlinear stages. Experimental data covering the transition regime for a high-speed flat-plate boundary layer are still not available, although some progress is being made for cone geometries (Stetson & Kimmel 1992, 1993). The flow parameters were chosen to match the secondary instability investigations of Ng & Erlebacher (1992) and are shown in table 1. These parameters resemble in essence the experimental setup of Kendall (1967).

A second-mode primary instability wave near branch II of the neutral curve with a streamwise wavenumber $\alpha = 2.52$ is excited initially with an amplitude of 0.4% with respect to the maximum streamwise velocity fluctuation (corresponding to a 6% maximum temperature fluctuation). Ng & Erlebacher (1992) found no evidence of

Re_{ξ_0}	9.1331×10^5
T^*_∞	61.15 K
T_W	4.38
δ_0	1.41
L_x	4.9867
L_y	2.9920
L_z	15.0

TABLE 1. Simulation parameters.

a fundamental secondary instability at these parameters. The present DNS results confirm this observation, since the $(2, \pm 1)$-modes remain at low amplitudes during the phases of linear and weakly nonlinear interactions to be defined below, figure 3. Since the secondary instability is initiated by a finite-amplitude primary wave, it is reasonable to choose a primary wave near branch II where its amplitude due to linear amplification in a spatially evolving flow would be a maximum. The most unstable subharmonic secondary instability wave with wavenumbers $\alpha = 1.26$ (streamwise) and $\beta = 2.1$ (spanwise) is allowed to grow from random noise superimposed with an amplitude of 10^{-5}. No spanwise symmetry is forced. Initially a computational mesh of $12 \times 12 \times 101$ gridpoints is used, which is refined later up to $128 \times 128 \times 191$ points. The simulation consumed about 140 hours of CPU time on a CRAY Y-MP C90. The code is completely vectorized and runs at about 500 MFLOPS using one Y-MP C90 processor. The present simulation was halted because of a CPU-time limitation and a need to rearrange the grid point distribution in the wall-normal coordinate taking into account that at the final stage the boundary layer has thickened by about a factor of 2. However, the simulation has been continued well into fully developed turbulence by Guo *et al.* (1994).

3.1. *Linear and nonlinear disturbance evolution.*

For an assessment of the disturbance growth a mode energy $E(k_x, k_y; t)$ is used which is defined as the magnitude of the Fourier-transformed velocity vector integrated over z:

$$E(k_x, k_y; t) = \int_0^{z_{max}} \hat{u}_j(k_x, k_y; t) \hat{u}_j^\dagger(k_x, k_y; t)\, \mathrm{d}z \tag{3.1}$$

(the dagger † denotes a complex conjugate). An overview of the temporal development of the leading modes and some higher harmonics is obtained from figures 3 and 4. As can be seen from figure 3, the primary wave, mode $(2, 0)$, grows initially with its linear growth rate $\omega_i = 0.0028$ for about 100 periods $T_\omega = 2\pi/\omega_r = 2.7646$, where $\omega_r = 2.2727$ is the primary wave frequency. At about $25 T_\omega$ the secondary instability modes $(k_x, \pm 1)$ start to evolve from background noise. At this time the amplitude of the primary wave has increased up to about $u''_{max} = 0.005$ (the double prime refers to a deviation from (x, y)-plane averages). The secondary wave growth rate at this primary wave amplitude, calculated from secondary instability theory, is $\sigma = 0.0292$ (secondary instability data by C.D. Pruett, private communication). Although several simplifying assumptions of the secondary theory (e.g. the shape assumption, frozen primary wave amplitude) are not enforced in the DNS, this value is close to the growth rate found in the simulation between $195 \leqslant t \leqslant 270$, which is 0.029 ± 0.001. The frequency of the subharmonic mode is 1.35 ± 0.002 for the $(1, 1)$-mode, which is also close to $\omega_r/2$ from theory. Note that the reference frame of the simulation

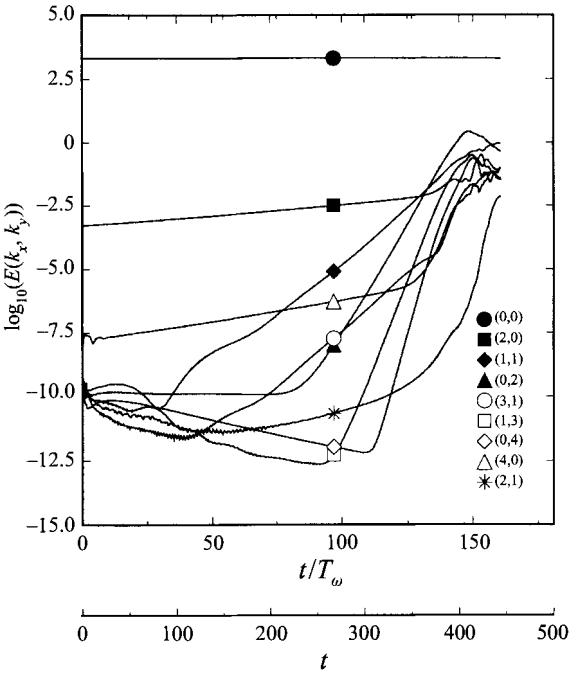

FIGURE 3. Temporal evolution of the mode energy for selected modes.

is at rest, so that the secondary frequency does not vanish. Primary and secondary modes travel downstream with a common velocity. This phase-locking yields the most effective environment for wave interaction.

After about $85T_\omega$ the correct secondary eigenfunctions can be extracted from the flow field, figure 5. A comparison with the results of the secondary instability theory for a primary wave amplitude of 0.5% demonstrates that the distributions of amplitude and phase (not shown) of the eigenfunctions agree well. The eigenfunctions have been normalized by the temperature maximum. About $80T_\omega$ after the onset of the subharmonic wave growth weakly nonlinear interactions take place which satisfy the conditions of nonlinear resonance (Drazin & Reid 1981, pp. 392–398). A strongly nonlinear interaction between the dominant modes sets in later at about $130T_\omega$, where the mode energy of the $(0,2)$-mode overtakes the $(1,1)$-mode. The $(0,\pm2)$-modes remain dominant during breakdown.

The rapid fill-up of the mode-energy spectrum is evident from a series of carpet plots in figure 6. At $t = 0$ the basic flow, the $(0,0)$-mode, and the primary wave, the $(2,0)$-mode, are visible standing out above the background noise, figure 6(*a*). First the spectrum fills up due to weakly nonlinear mode interactions. Thus only modes with an even sum $k_x + k_y$ grow significantly, yielding a typical checkerboard nature of the spectrum, figure 6(*b*). Strongly nonlinear interactions of the 'even' modes lead to a strong increase of the global energy level, figure 6(*c*). After about $130T_\omega$ modes with an odd sum $k_x + k_y$ begin to grow at a nearly common growth rate, figure 4, which can be estimated to be about $\frac{1}{2}\,\mathrm{d}(\ln E)/\mathrm{d}t \simeq 0.16$. This is about 5.5 times larger than the secondary-wave growth rate. These 'odd' modes are not excited by nonlinear interactions among the even modes. However, with the onset of strongly nonlinear interactions accompanied by the evolution of pronounced vortex

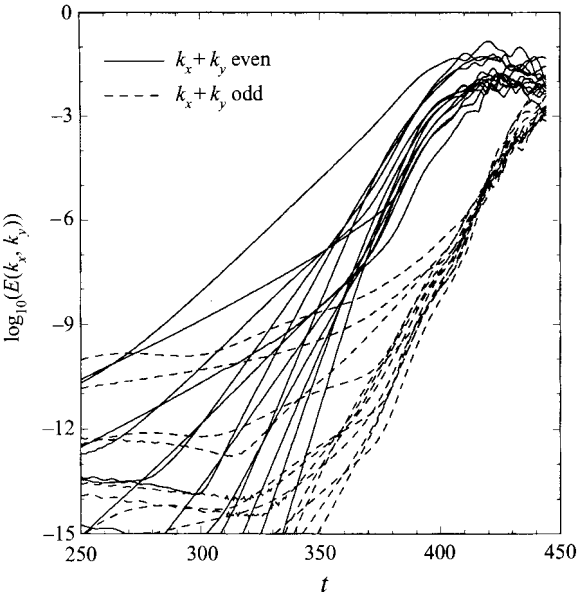

FIGURE 4. Temporal evolution of mode energy of even and odd modes at late stages.

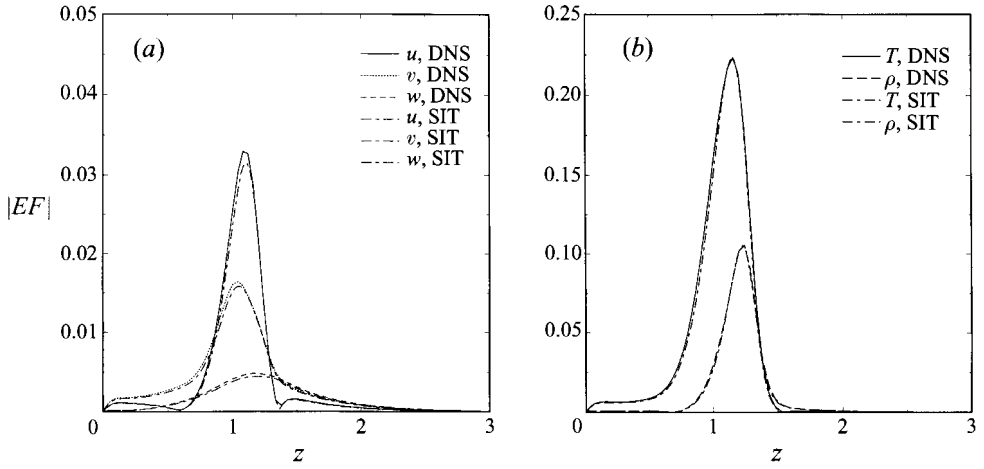

FIGURE 5. Comparison of secondary wave amplitude functions between secondary instability theory and DNS, $t = 235.16$. (*a*) u, v, w (*b*) T, ρ.

and shear-layer structures (see subsequent sections), the odd modes become highly amplified and grow rapidly from background noise and round-off error level.

At the final state of the present simulation the even modes are saturated at an energy level which is nearly attained by the odd modes, figure 4. Thus the spectrum has lost its checkerboard nature and is close to a turbulent one, figure 6(*d*). The energy spectrum is used to estimate the resolution requirements throughout the simulation. Note that even at the final stages the spectrum decays by at least seven orders of magnitude, so that the present resolution is considered to be sufficient.

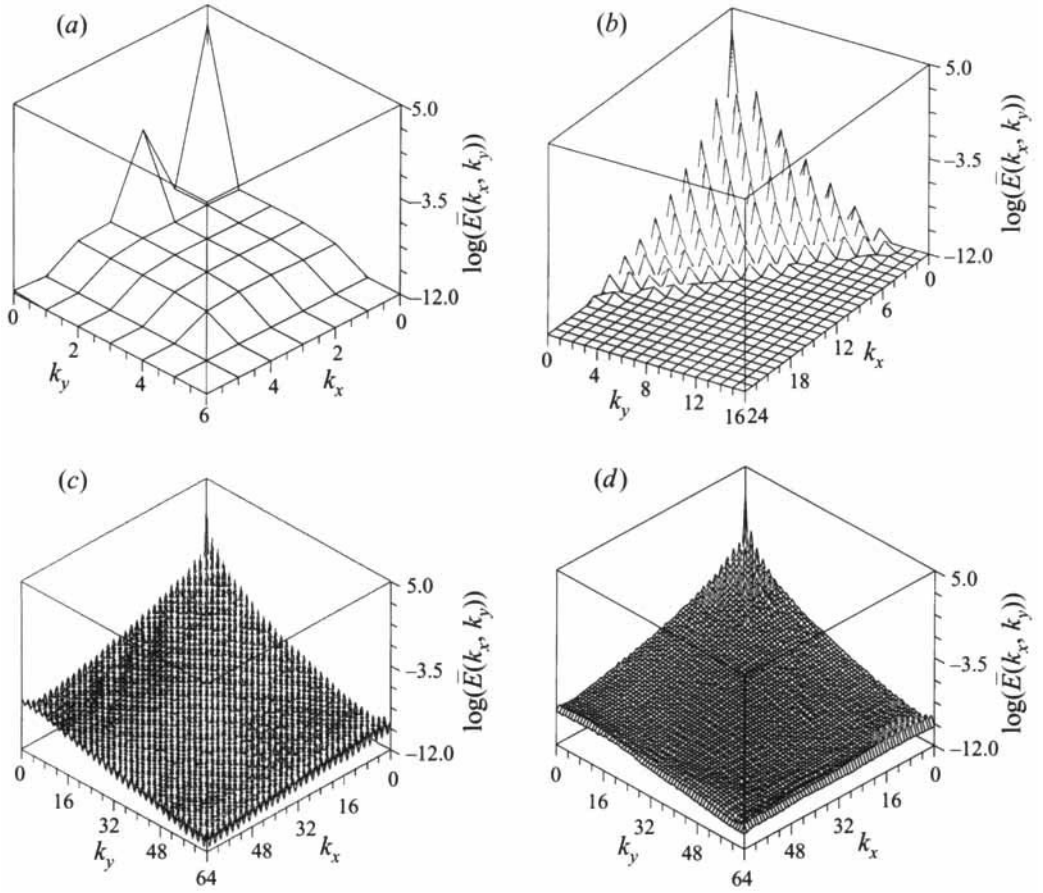

FIGURE 6. Carpet plots of mode energy at different times. (*a*) $t = 0$, (*b*) $t = 368.13$, (*c*) $t = 424.48$, (*d*) $t = 440.60$.

3.2. *Formation of Λ-vortices*

In a frame of reference moving with the phase velocity the primary wave appears as a set of spanwise vortices located near the critical layer shown in figure 7 in terms of iso-pressure surfaces. The low-pressure cores near the critical layer represent the spanwise vortices, which are slightly perturbed by the imposed noise (the noise amplitude is modulated by the function $z^2\exp(-z^2)$, so that the perturbation near the wall is invisibly small). The low-pressure regions near the wall, shifted by half a wavelength relative to the critical-layer perturbation vortices, are due to the pressure wave reflection between the wall and the relative sonic layer at $z = 0.55$ where the convective Mach number $M_c := M_\infty(u - c_{Phase})/T^{1/2}$ equals -1. A schematic of this process, suggested by Morkovin, can be found in Mack (1990). A visualization of the second-mode wave is provided in figure 8. For this purpose the laminar mean flow has been superimposed with a second-mode wave of an amplitude of $u''_{max} = 5\%$. At the sonic layer ($z = 0.55$) the second-mode wave changes its character from an acoustic to a vorticity mode. The sonic layer experiences a sinuous perturbation by the small vortices near the critical layer at $z_c = 1.08$. Thus a compression wave propagates from each local minimum of the relative sonic u-isotaches to the wall and is reflected back and forth following the reflection laws in supersonic flows.

In the relative subsonic region above the sonic layer the secondary instability

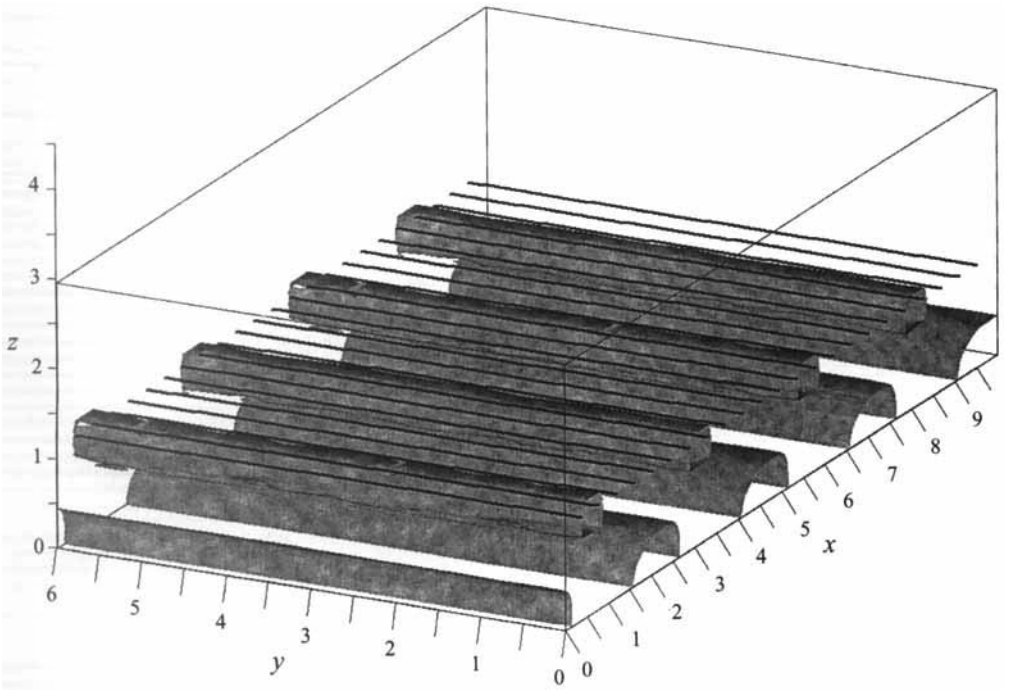

FIGURE 7. p-iso-surfaces ($p = 0.03515$) and vortex lines at $t = 0$. Data duplicated periodically in the streamwise and spanwise directions.

deforms the primary-wave spanwise vortices and a staggered pattern of Λ-vortices emerges, as visualized in figure 9. Since the primary wave travels downstream at about 90% free-stream velocity the critical layer is located near the laminar boundary-layer edge ($\delta_0 = 1.41$, based on 99.9% free-stream velocity). This region possesses low mean shear and is decoupled from wall effects by the sonic layer. Thus low-subsonic inviscid effects may become responsible for the primary-vortex deformation.

Self-induction moves the Λ-vortex tips upward and the vortex tails downward. Thus by mean shear the downstream velocity difference along a vortex leg increases and the vortex is stretched considerably in the streamwise direction, figure 10. Also, presumably by interaction of inductive deformation and mean shear, the Λ-vortex becomes S-shaped and twisted. Just below the Λ-vortex legs pronounced high- and low-velocity streaks in the streamwise velocity appear, which are represented by the $(0, 2)$-mode in spectral space.

A remark about visualization of large-scale vortical structures is in order. Vortices are basically identified herein by iso-surfaces of low pressure, as done e.g. by Sandham & Reynolds (1991). Low pressure turned out to be most useful for the identification of vortices, particularly at highly nonlinear stages. Other criteria, such as invariants of the rate-of-deformation tensor or its discriminant, were mostly not sharp enough. The same experience has been reported in Sandham & Kleiser (1992) and the reader is referred to this paper for a discussion of the different criteria. A justification may come from compressible viscous vortex similarity solutions, where the vortex core is shown to possess a strong local pressure minimum (Mayer & Powell 1992). In the current work the coincidence of pressure minima and vortex cores has always been verified by an additional necessary criterion, usually that of a positive discriminant of the characteristic equation of the velocity-gradient tensor (Vollmers, Kreplin &

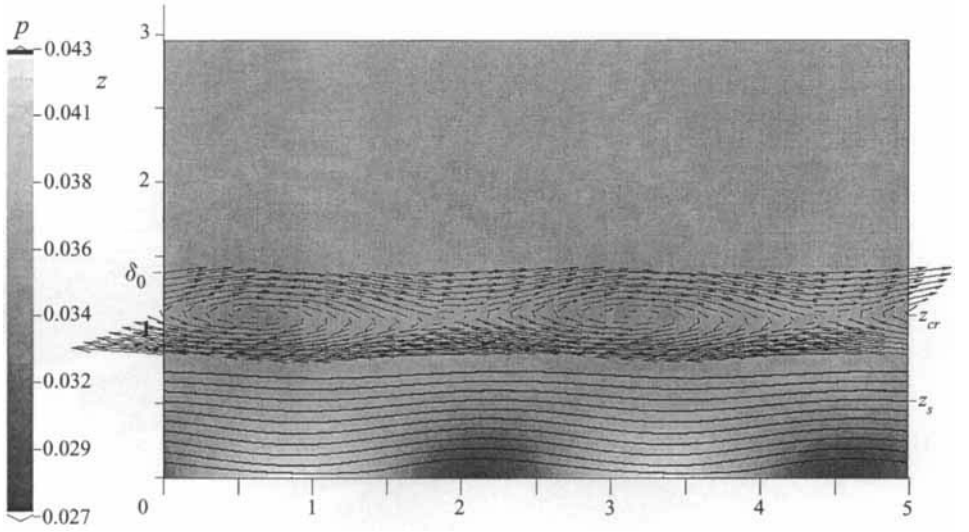

FIGURE 8. p-values, u-contours and velocity vectors due to a second-mode instability wave in a moving reference frame. δ_0 indicates the boundary-layer thickness, z_{cr} the position of the critical layer and z_s the sonic layer.

Meier 1983). In cases where the vortex-axis was approximately known in advance, the equivalence of local pressure minima and vortex cores was also verified by examining streamlines of the cross-flow. These streamlines should appear as foci in a plane approximately perpendicular to the vortex axis. A comparison of these different criteria for locating the Λ-vortex is shown in figure 11. It is evident that pressure minima and cross-flow foci coincide, as do pressure minima and positive values of the discriminant D.

3.3. *Formation of Y-shaped shear layers*

An important new element in the transition process at this stage is shear layers generated by the Λ-vortices. Each shear layer is Y-shaped with the stalk pointing upstream and is located below and between two neighbouring Λ-vortices, as can be seen in figure 12. It is supposed that the Stuart mechanism (Stuart 1965) is responsible for the shear-layer generation. In the present configuration the lower shear layers do not build up at the wall but above the sonic layer. Using Stuart's terminology the Y-shaped shear layer can be considered as the detached shear layer at the lower ('valley') position. It is found from corresponding iso-contour plots of spanwise vorticity and density (not shown) that the detached lower shear layers coincide with regions of high density variation. An upper ('peak', Stuart 1965) shear layer also exists, but remains only weakly developed during the early phase of breakdown. This shear layer evolves in a peak plane which coincides with a plane of symmetry of the Λ-vortices and is located slightly above the laminar boundary-layer edge, figure 13(a). Thus it is in a region of weak mean shear and remains almost inactive during the first phase of breakdown.

In figure 13(a), closer to the wall, a cut through the stalk of the Y-layer is visible from iso-contours of spanwise vorticity. Note that the detached shear-layer evolution is confined to the relative subsonic domain of the boundary layer, shown with dashed lines in figure 13(b). The presence of a detached shear layer below the Λ-vortex, but well above the wall, is different from boundary-layer transition in incompressible flow,

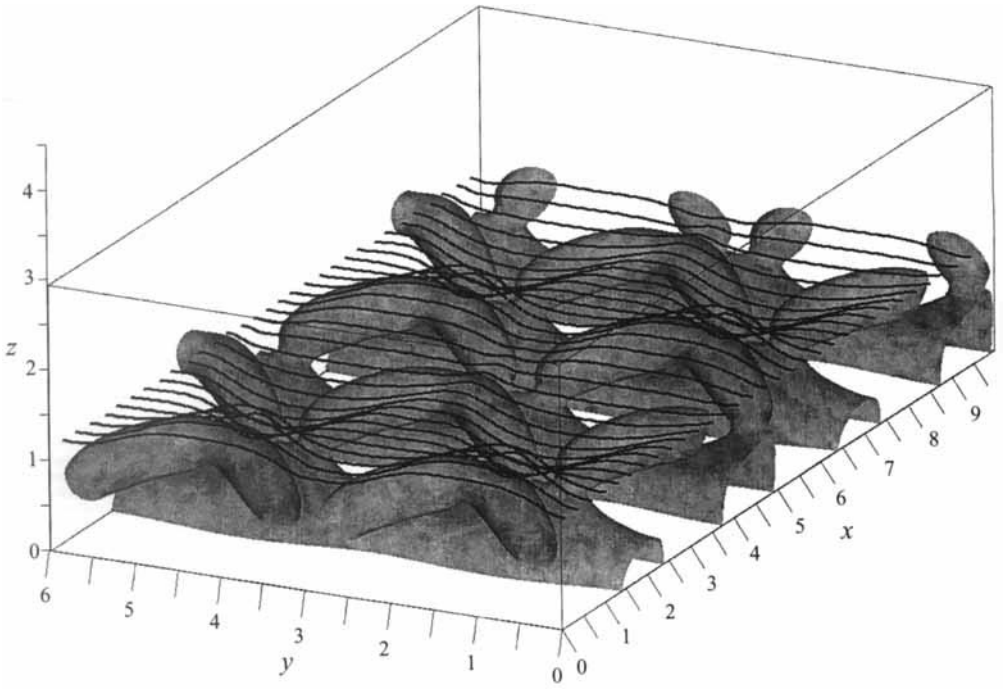

FIGURE 9. p-iso-surfaces ($p = 0.03475$) and vortex lines at $t = 368.13$. Data duplicated periodically in the streamwise and spanwise directions.

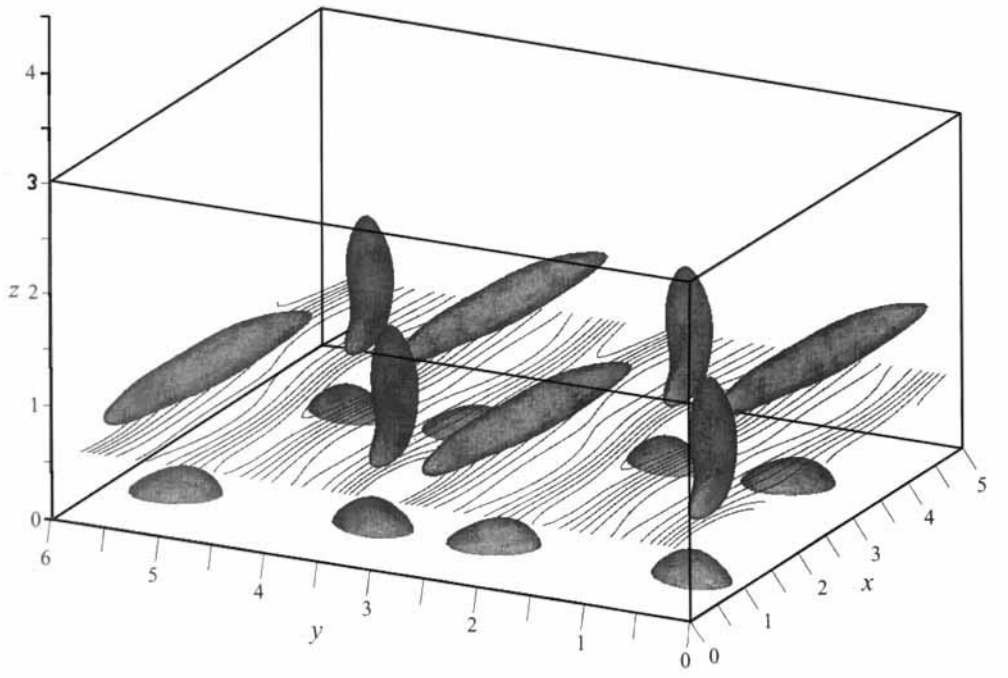

FIGURE 10. p-iso-surfaces ($p = 0.03237$) and contours of streamwise velocity u in a plane $z = 0.63$ at $t = 392.70$. Data duplicated periodically in the spanwise direction.

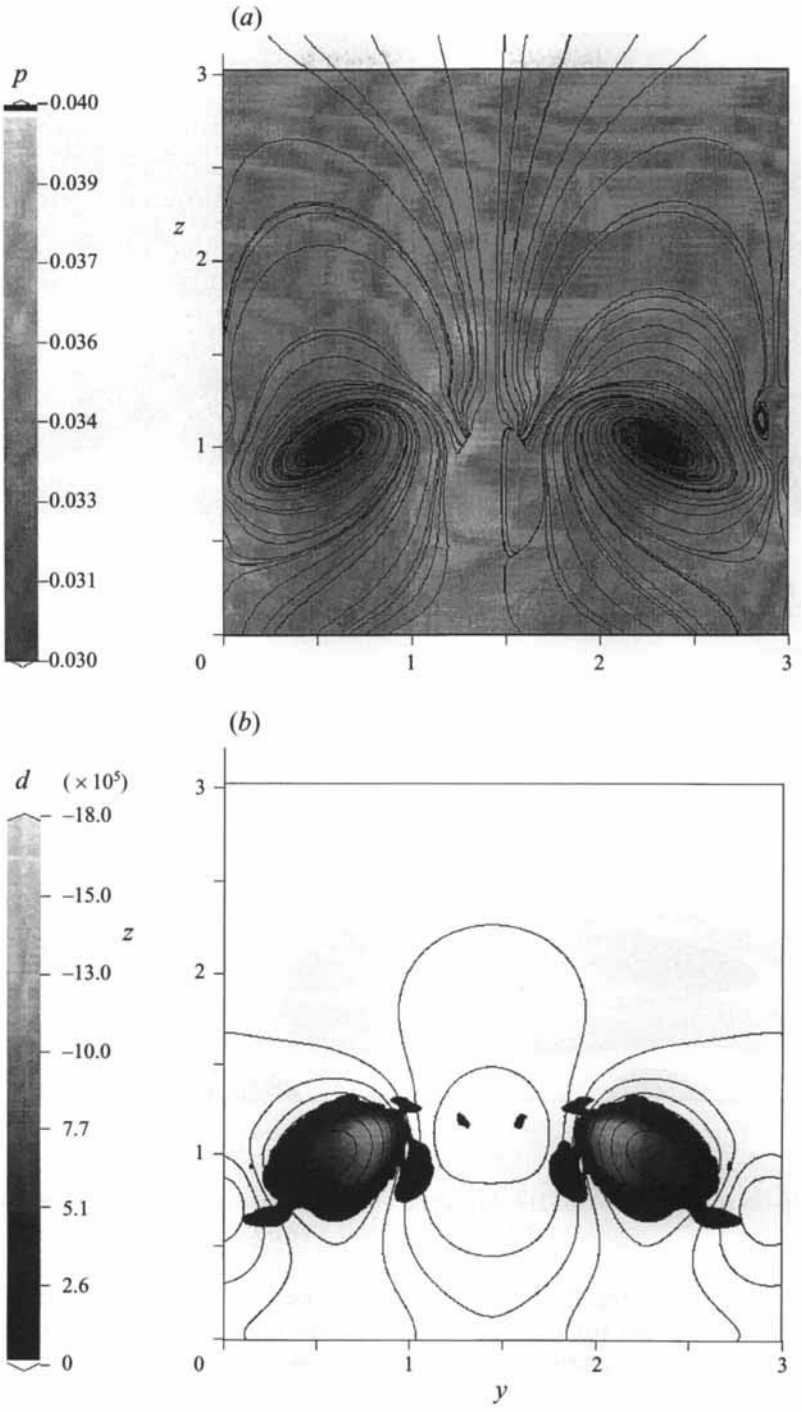

FIGURE 11. Cross-section at $x = 1.56$ and $t = 392.70$. (*a*) p-values and cross-flow streamlines, (*b*) p-contours and discriminant D.

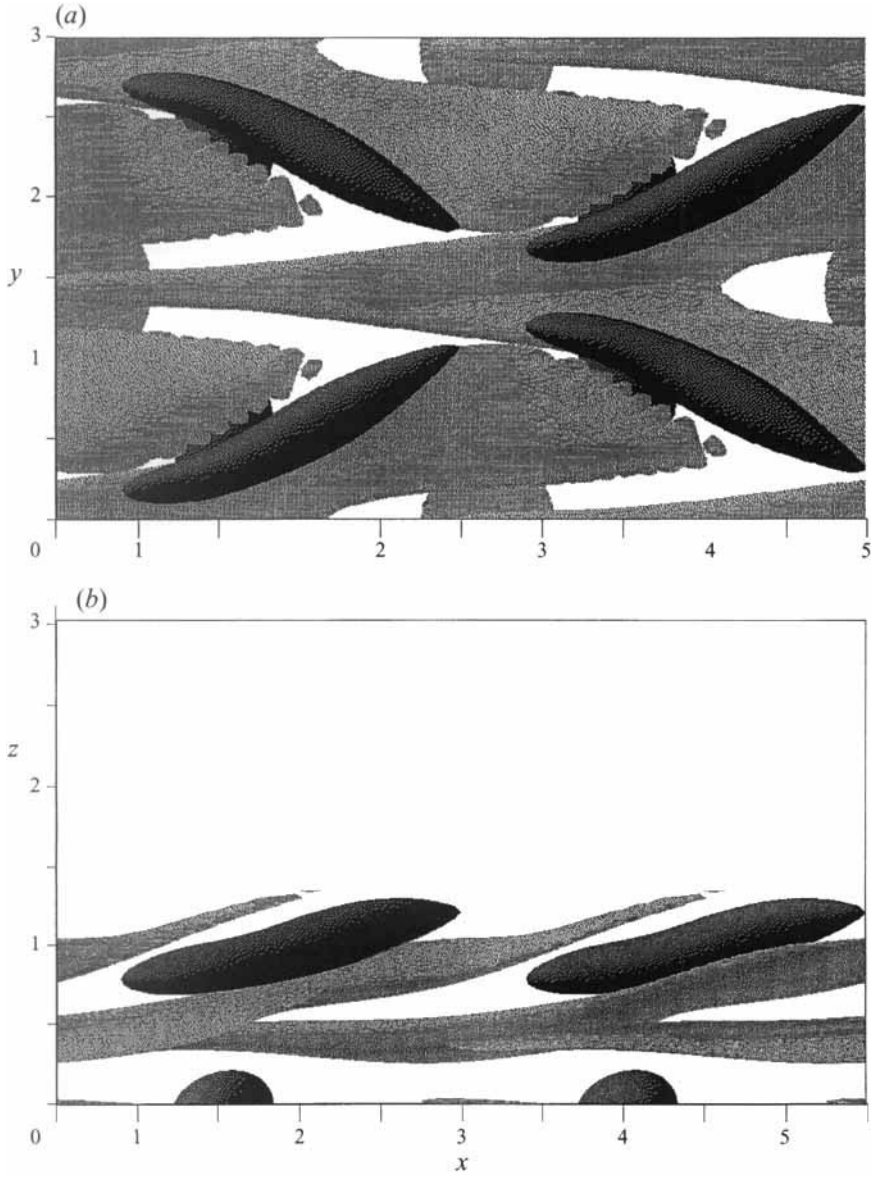

FIGURE 12. p-iso-surfaces ($p = 0.03237$, dark) and ω_y-iso-surfaces ($\omega_y = 1.4$, light) at $t = 392.70$. (a) Top view, (b) side view.

where several roll-up stages of an upper detached shear layer can be observed but no lower shear layer (except for the near-wall vorticity layer) exists. An adaptation of the Stuart mechanism for compressible flow is discussed in §4.

3.4. *Shear-layer break-up*

The shear layers gain strength, and become elongated and distorted. In a peak plane the upper shear layer moves outwards and parts of the Y shear layer move towards the wall. Near the branch of the 'Y', which is located close to the centre of the corresponding Λ-vortex leg, the shear layer begins to roll up first. Close to the wall the spanwise vorticity lines up in streamwise streaks, two per secondary spanwise

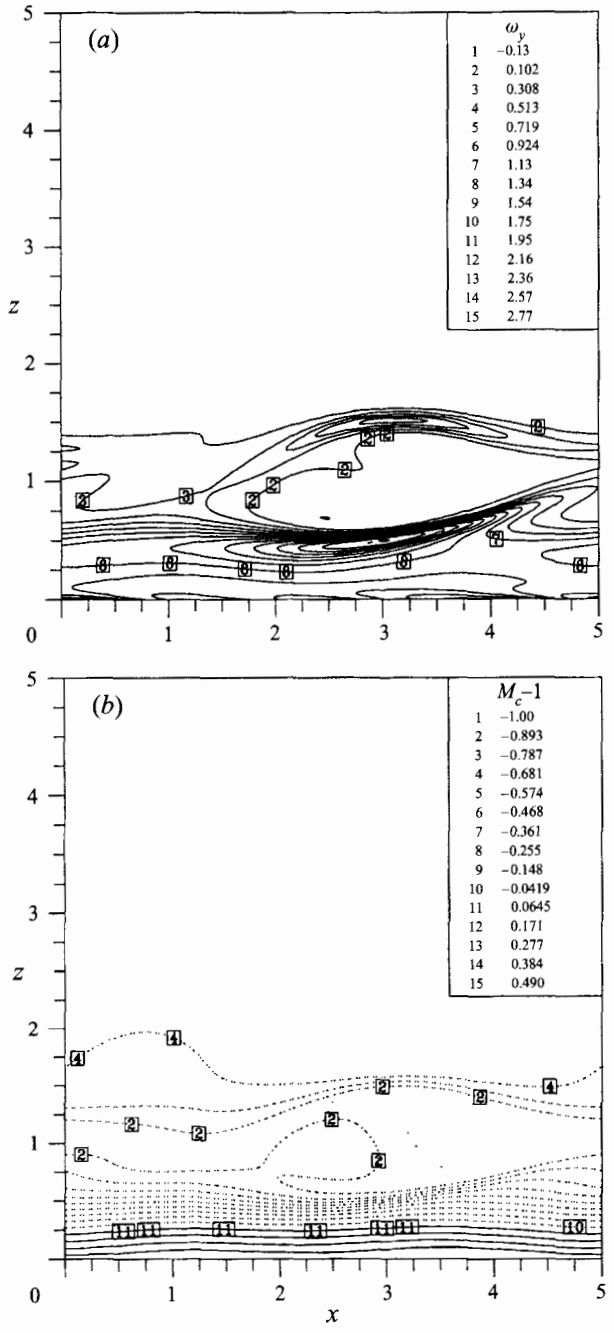

FIGURE 13. ω_y- and M_c-contours in a peak plane $y = 1.45$ at $t = 392.70$. (*a*) ω_y-contours, (*b*) M_c-contours.

wavelength (Adams & Kleiser 1993*a*). The Y-shear-layer roll-up is connected with the formation of a new set of smaller-scale vortices. The axes of the Λ-vortices enclose an angle of about 45° with the streamwise direction and are inclined at about 15°. The first roll-up vortices, denoted as L1, are oblique at about 40° and are not inclined. Their cores are still visible at $t = 411.79$ from the ellipsoidal low-pressure regions

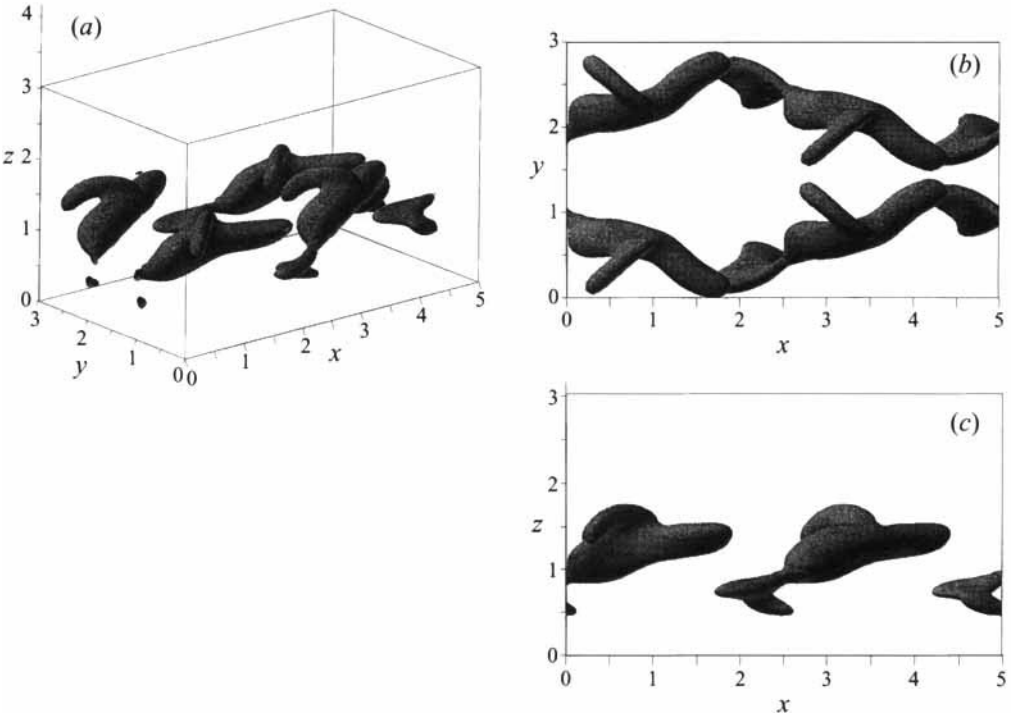

FIGURE 14. p-iso-surfaces ($p = 0.03$) at $t = 411.79$, L2-roll-up of the Y-shear-layer. (a) Perspective, (b) top-view, (c) side-view.

below the former centres of the corresponding Λ-vortex leg, for instance at $x \simeq 2.2$, $z \simeq 0.5$ in figure 14(c). Near the locations where the L1-vortices appear, the upstream parts of the Λ-vortices are torn off. They are swept towards the wall and become weak, so that they cease being visible as pronounced low-pressure cores in figure 14.

When the tips of the Y-layer reach the preceding Λ-vortex the second roll-up L2 is observed. It is evident from a shear-layer deflection near a local spanwise vorticity maximum in an (x,z)-plane at $x \simeq 1.3$, $z \simeq 1.3$ or $x \simeq 3.8$, $z \simeq 1.3$, figure 15(a). The second roll-up vortices are visible as horn-like iso-pressure surfaces, figure 14(a). Looking from above they form an inverted Λ-pattern with an enclosed angle of about 80°, figure 14(b). Besides the upper shear layer, a second-generation shear layer is also visible in a peak plane which traverses the boundary layer at an inclination of about 45°, figure 15(b). It is a result of low-speed fluid, lifted up by induced motion of the L1-vortices.

Since high-speed fluid is convected towards the wall in the mean, the velocity difference between the bottom and top regions of the vortices decreases and the inclination of the vortical structures becomes larger, figure 16(b). In an off-peak plane fragments of the Y-shear-layer can be seen. The rolled-up tip has moved outwards and the remnants of the L1 roll-up are still visible as weak local ω_y-maxima at $x \simeq 1.2$, $z \simeq 0.5$ and $x \simeq 3.7$, $z \simeq 0.5$. Also new maxima are present now at $x \simeq 2.1$, $z \simeq 0.6$ and $x \simeq 4.6$, $z \simeq 0.6$. They indicate the third roll-up stage L3 which generates a new set of vortices below the Λ-vortices near the centre of their leg, figure 17. The remnants of the Λ-vortices now enclose an angle of 45° and are still inclined at about 15°.

Similar to the L1-vortices, the L3-vortices again tear off an upstream-pointing part

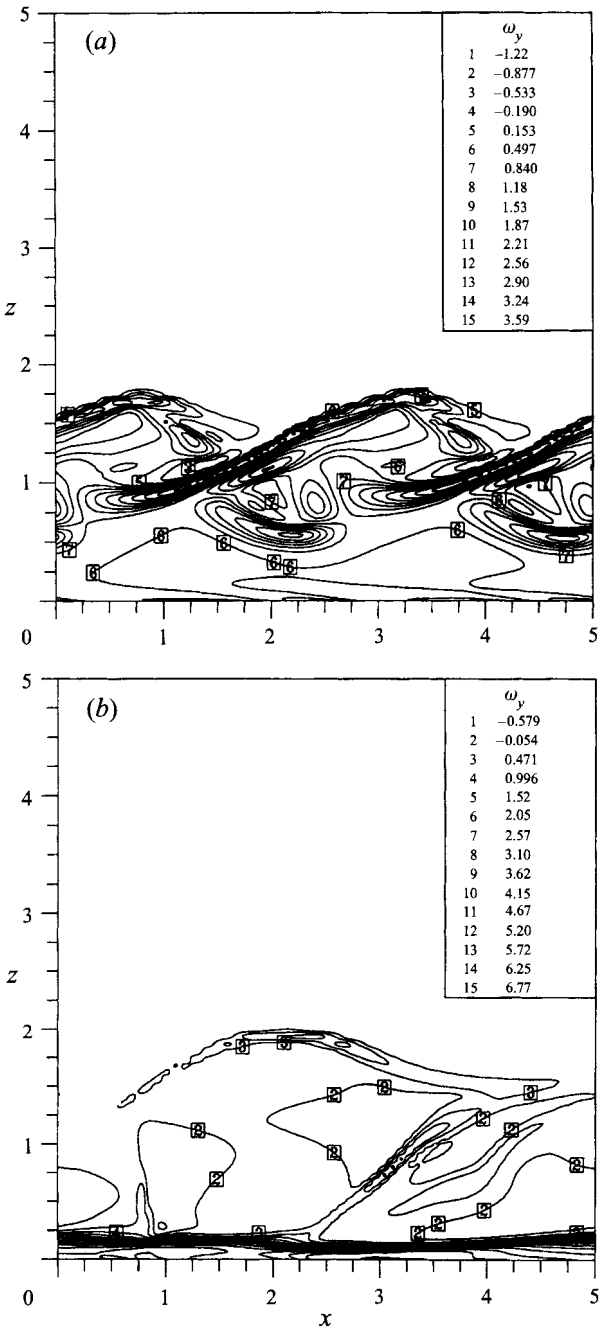

FIGURE 15. ω_y-contours at $t = 411.79$, L2-roll-up of the Y-shear-layer. (*a*) Off-peak plane at $y = 0.70$, (*b*) peak plane at $y = 0$.

of the Λ-vortices. These fragments move towards the wall and build up a pair of counter-rotating streamwise-aligned vortices. Low-speed fluid convected upwards by these streamwise vortices generates a second-generation shear layer. From its roll-up a cylinder-shaped vortex LU1 results. The head-region of the former Λ-vortex resembles a smaller Λ-vortex.

With the appearance of the first roll-up stage of the upper shear layer U1, visible

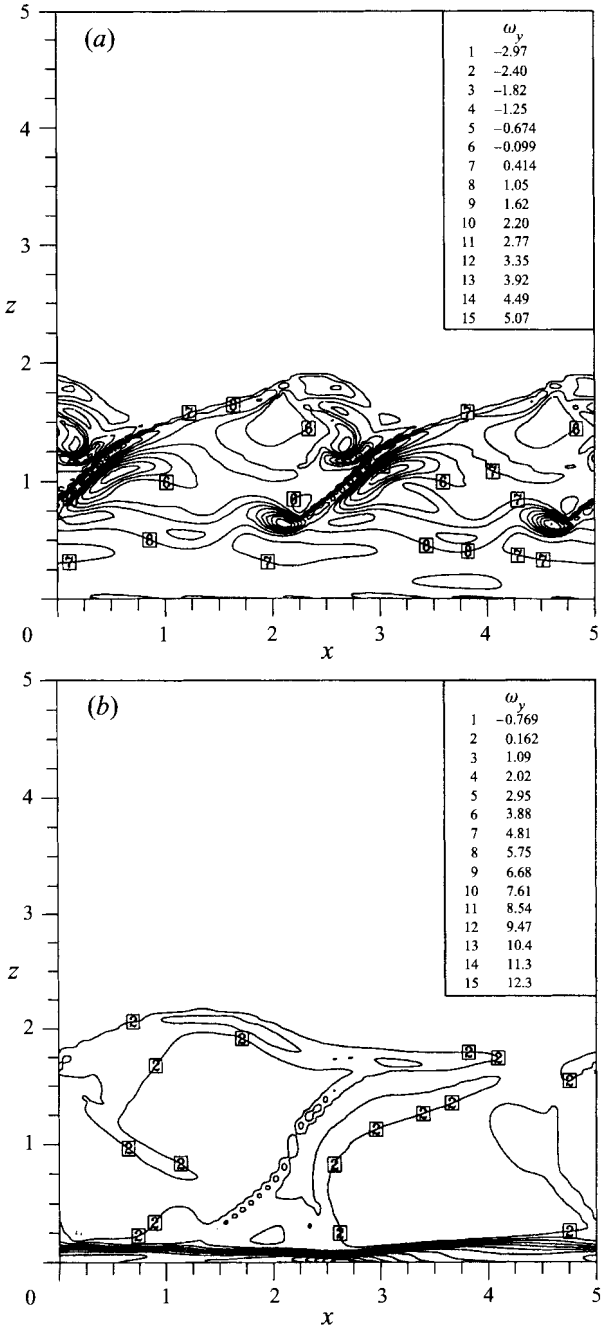

FIGURE 16. ω_y-contours at $t = 416.55$, L2-roll-up of the Y-shear-layers. (*a*) Off-peak plane at $y = 0.70$, (*b*) peak plane at $y = 0$.

from the ω_y-contours at a peak-plane at $x \simeq 3.5$, $y \simeq 2.3$ at figure 18(*a*), new structures of decreasing size can be observed within decreasing time intervals. The U1 roll-up stage of the upper shear-layer is one of the last events which can be captured distinctly from the simulation data. At $t = 427.48$ it is visible as an arch-like vortex in $x \simeq 4$, $z \simeq 2.3$, figure 19. At this time the upper shear layer has undergone a

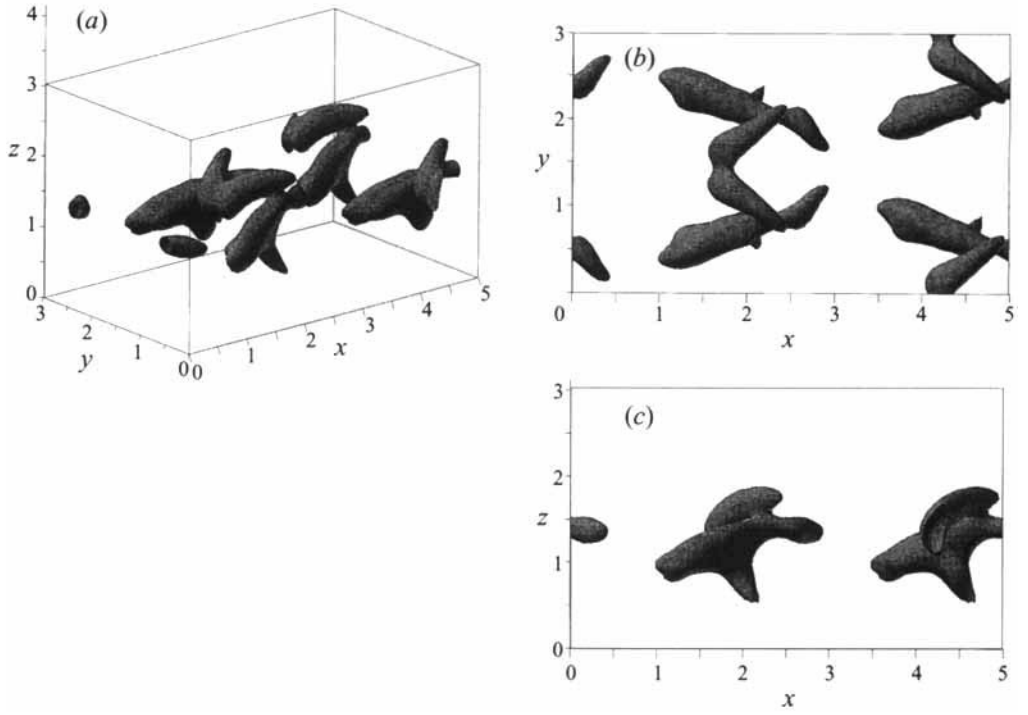

FIGURE 17. p-iso-surfaces ($p = 0.028$) at $t = 416.55$, L3-roll-up of the Y-shear-layer. (a) Perspective, (b) top-view, (c) side-view.

second roll-up generating a barrel-shaped vortex U2 at $x \simeq 2.7$, $z \simeq 2.3$. Also the LU1-vortices are visible, for instance at $x \simeq 0.8$, $z \simeq 1.8$. We note that arch- and barrel-shaped vortices are known to exist during the detached shear layer evolution in incompressible transition, see for example Sandham & Kleiser (1992). In a peak-plane, figure 18(a), a strong near-wall shear layer, stemming from the Y-layer fragments, has also built up. It is separated from the upper shear layer by a region of weak vorticity fluctuations. The break-up of the Y-layer, which is confined to a rather close vicinity of the off-peak planes, has now experienced the fourth roll-up stage. These L4-vortices show up as C-shaped structures, which extend from $z \simeq 1.2$ to $z \simeq 1.8$, in the middle region of the boundary layer, figure 19. The generation mechanism of the L4-vortices is quite similar to that of the L1- and L3-roll-ups. However, their shape is different since the shear layer has been wrapped around the small Λ-vortices originating from the head regions of the original Λ-vortices.

The further development becomes increasingly complex, in part due to interactions of the Y-layer roll-up vortices Ln, formed at off-peak planes, and upper-shear-layer roll-up vortices Un, formed at peak planes, and cannot be described in detail here. However, a few remarks about some of the most prominent observations are in order. The arch-like vortices U1 from the first upper-shear-layer roll-up evolve into a hairpin vortex. The interactions between Ln-vortices and Un-vortices mentioned previously now cause a spreading of vorticity fluctuations between peak and off-peak planes such that significant fluctuations can also be observed in the middle region of a peak plane.

Isolated hairpin vortices have the tendency to form vortex loops as has been shown by Moin, Leonard & Kim (1986). Nearly perfect vortex loops, which have obviously

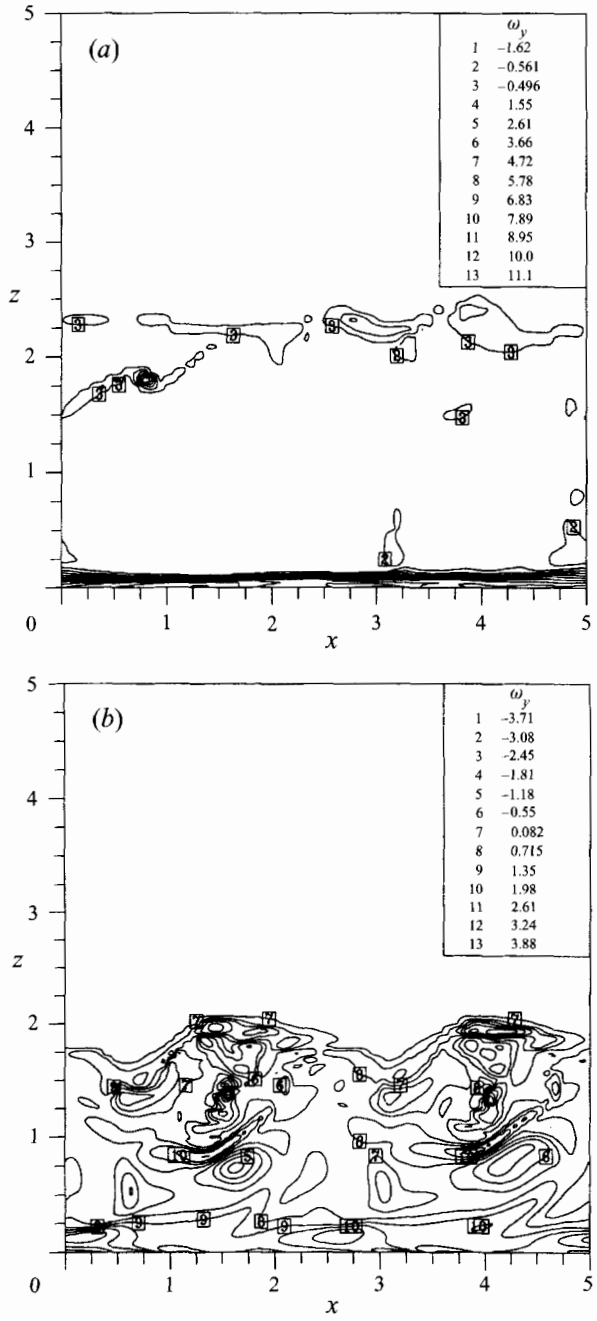

FIGURE 18. ω_y-contours at $t = 427.48$, L4-roll-up of the Y-shear-layer, U1- and U2-roll-up of the upper shear-layer. (*a*) Peak plane at $y = 1.45$, (*b*) off-peak plane at $y = 0.70$.

evolved from the former hairpin vortices, can be found at $t = 440.46$ in the outer region of the boundary layer at the peak planes, figure 20. The vorticity distribution in the peak and off-peak planes becomes more and more irregular, figure 21. In particular the initial streamwise periodicity due to the primary wave is entirely lost now in both the peak planes and the off-peak planes. The vortical structures near the

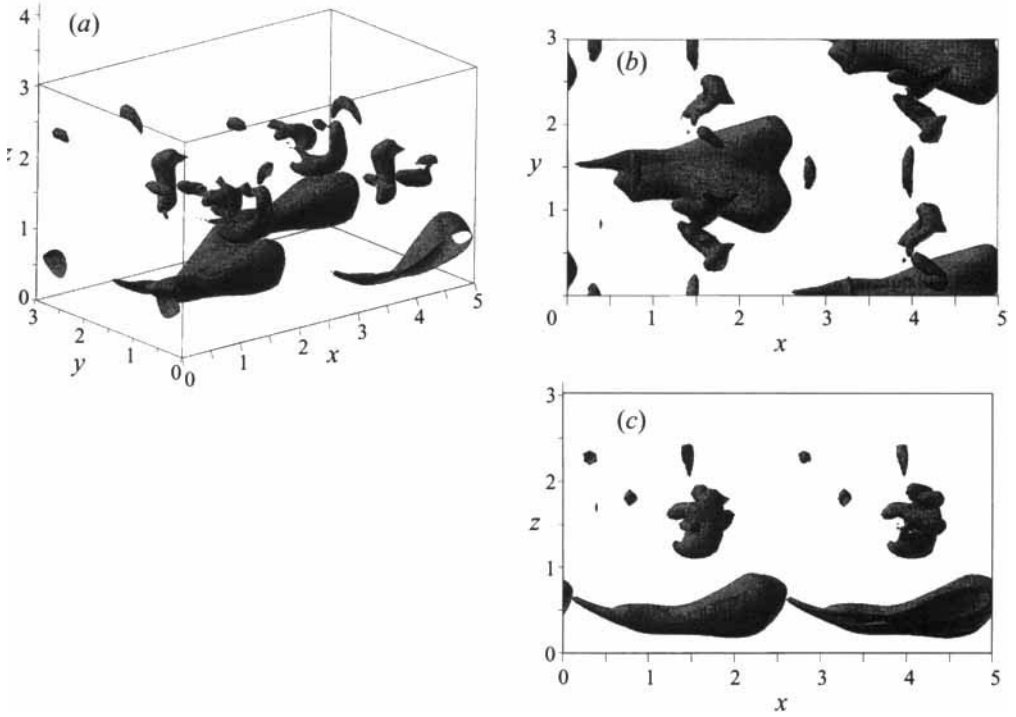

FIGURE 19. p-iso-surfaces ($p = 0.03$) at $t = 427.48$, L4-roll-up of the Y-shear-layer, U1- and U2-roll-up of the upper shear-layer. (*a*) Perspective, (*b*) top-view, (*c*) side-view.

wall are nearly aligned in the streamwise direction, figure 20. In the middle region of the boundary layer they are inclined at about 45° to 50° and in the outer region at 70° to 90°. This is agrees with the experimental results by Spina & Smits (1987) for a turbulent boundary layer at $M_\infty = 3$.

3.5. *Spreading of the disturbances*

The secondary eigenfunctions possess amplitude maxima near the critical layer. The maximum fluctuations thus originate at the critical layer and spread both towards the wall and towards the boundary-layer edge. To illustrate this development, in figure 22 the grid points with $\tau'_{11} \simeq 0.001$ are traced with t, where $\tau'_{11} = \overline{\rho u'_1 u'_1}$. The overbar denotes an average in the (x, y)-plane, the tilde a Favre-average (mass-weighted) in the (x, y)-plane and the primed quantities are fluctuations with respect to Favre-averaged mean quantities, $u' = u - \overline{\rho u}/\bar{\rho}$. In the (z, t)-plane a wedge evolves with an aperture of about $\phi_1 = 1.7°$ towards the wall and about $\phi_2 = 1°$ outwards. Obviously the wall-normal spreading sets in at the stage of the shear-layer build-up. With the onset of the Y-layer break-up the outward spreading angle increases to $\phi_3 \simeq 2°$. The spreading wedge extends down to $z \simeq 0.028$ which corresponds to $z^+ = 4.6$ at $t = 440.46$, i.e. the edge of the viscous sublayer when calculated in instantaneous wall units.

By tracing the vortices in the peak and off-peak planes through their low-pressure cores it is found that the vortices in the upper part of the boundary layer move downstream with a velocity of $c_{vx} = 0.85$ which corresponds to 94% primary-wave phase velocity. As far as they can be captured accurately enough, this is also true for the Y-shear-layer roll-up vortices in the lower part of the boundary layer. In the later stages the streamwise vortices in the lower part of the boundary layer become

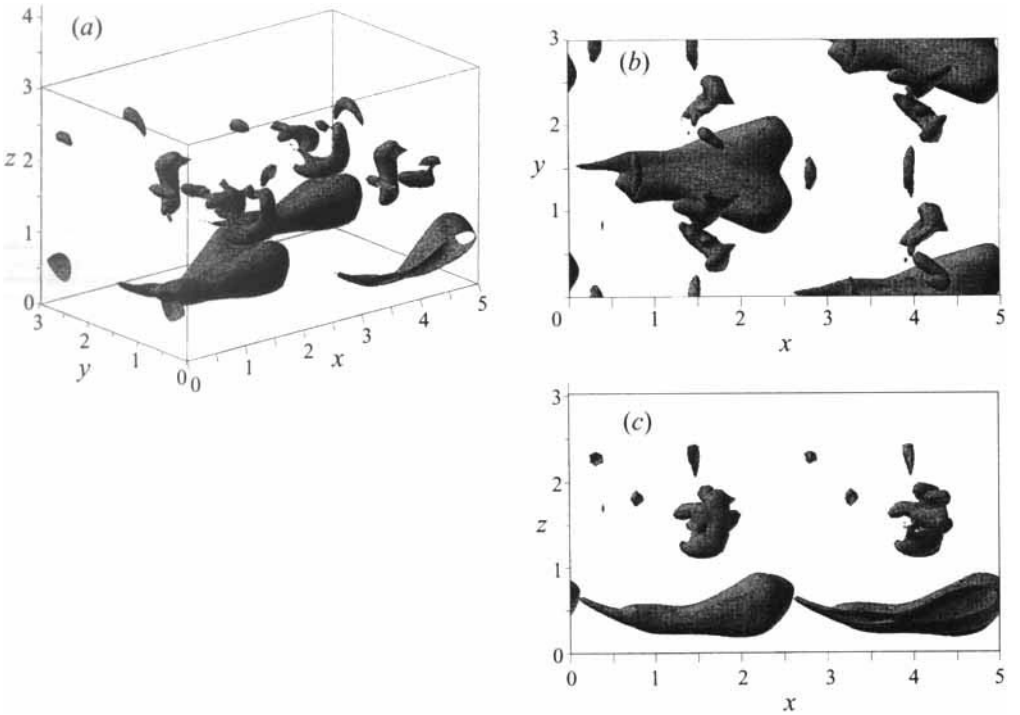

FIGURE 20. p-iso-surfaces ($p = 0.03$) at $t = 440.46$. (a) Perspective, (b) top-view, (c) side-view.

increasingly difficult to define since their pressure minima in (x, z)-planes become broader. The velocity of the outward motion is different for the Ln and Un vortices. While the Y-layer roll-up vortices Ln move upward and downward respectively at about $c_{vz} = 0.015$, depending on whether their initial position is above or below the critical layer, the Un and LU1 vortices move significantly faster outward at about $c_{vz} = 0.05$. It can be concluded that the fluctuations spread due to the wall-normal propagation of the vortical structures.

3.6. *Global evolution*

During the final stage of the simulation the spanwise symmetry, which has formed in the secondary instability stage, is lost gradually. A measure Σ_y of the spanwise asymmetry can be defined by the Euclidean norm of the mode-energy differences of corresponding spanwise harmonics (Adams 1993)

$$\Sigma_y = \left[\frac{4}{N_1 N_2} \sum_{k_1=0}^{N_1/2-1} \sum_{k_2=0}^{N_2/2-1} [E(k_1, k_2) - E(k_1, N_2 - k_2)]^2 \right]^{1/2}.$$

The spanwise asymmetry grows non-monotonically in time with a slightly increasing frequency, figure 23. This non-monotonic behaviour can be traced back to the asymmetric distribution of the initial background disturbances. Figure 24 shows the evolution of the mode energy of the mode $(1, 1)$ and its conjugate mode $(1, -1)$, which are the left- and right-going subharmonic waves. It is evident that these modes are phase-shifted by about π when they begin to grow from the noise level. The amplitude modulation caused by this phase shift reduces strongly with increasing time. After about $t \simeq 200$ the $(1, \pm 1)$-modes are practically identical with the subharmonic

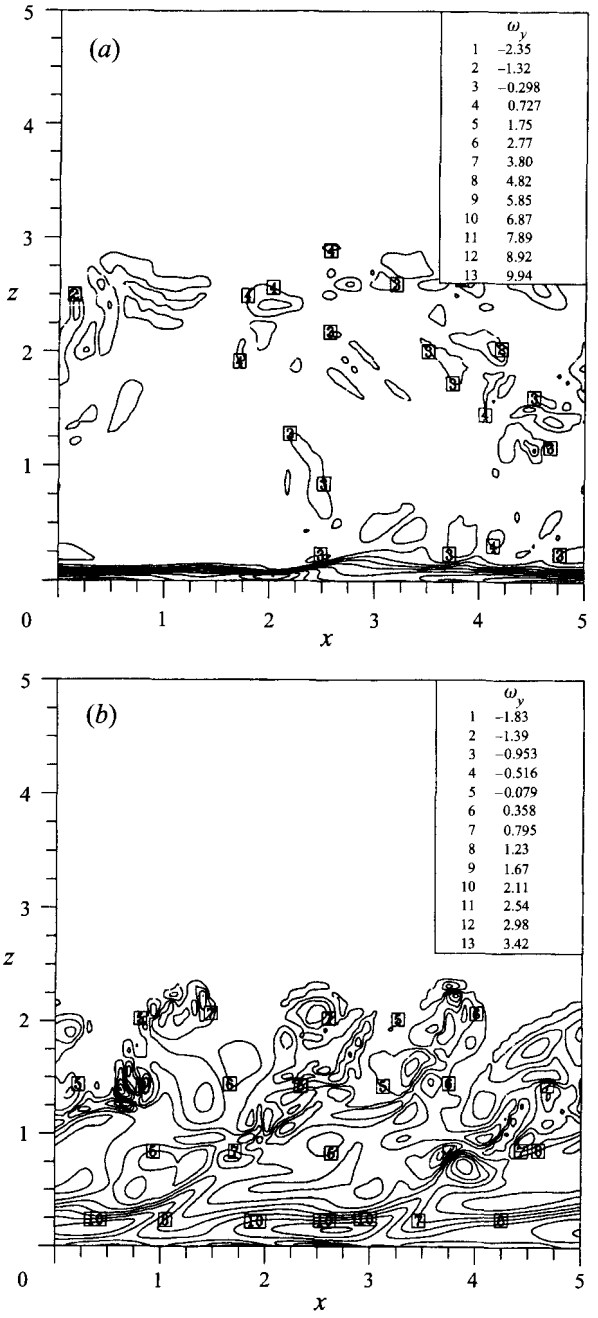

FIGURE 21. ω_y-contours at $t = 440.46$. (*a*) Peak plane at $y = 1.45$, (*b*) off-peak plane at $y = 0.70$.

instability modes. Nevertheless this amplitude modulation, which will be identified below as a superposition of damped waves upon the subharmonic waves, dominates the evolution of the spanwise asymmetry during the linear and the weakly nonlinear stages. Also it is noted that streamwise-averaged modes, for example the $(0, \pm 2)$-modes, are strictly symmetric. A simple model based on the concept of 'priming disturbances' of Kachanov & Levchenko (1984), adapted to the present temporal instability problem, can be formulated. It yields the following simple approximation

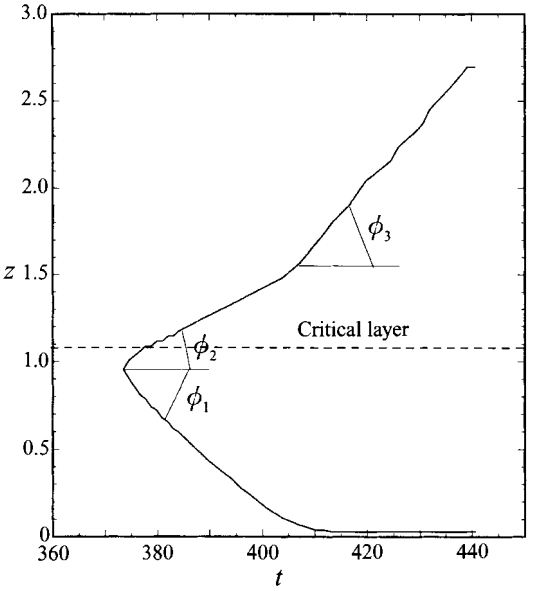

FIGURE 22. Spreading of fluctuations, $\tau'_{xx} \simeq 0.001$.

for the temporal behaviour of the $(1, \pm 1)$-mode amplitudes:

$$\left.\begin{aligned} \hat{A}_{1,1} &= \hat{A}_0 e^{\sigma_r t} e^{i\sigma_i t} \left(1 + e^{\chi t} e^{i(\phi t + \psi_{1,1})}\right) \\ \hat{A}_{1,-1} &= \hat{A}_0 e^{\sigma_r t} e^{i\sigma_i t} \left(1 + e^{\chi t} e^{i(\phi t + \psi_{1,-1})}\right) . \end{aligned}\right\} \tag{3.2}$$

The parameters in (3.2) can be estimated from the simulation as $\sigma_r = 0.028$, $\phi = 0.061$, $\psi_{1,1} = -\frac{2}{3}\pi$, $\psi_{1,-1} = -\frac{5}{3}\pi$, $\chi = -0.008$. The damping χ reduces the influence of the amplitude modulation term on the right-hand side with increasing time. The asymmetry evolution for the subharmonic modes resulting from this simplified model is in qualitative agreement with the Σ_y-evolution of the simulation results, figure 23.

The well-known increase of the skin friction coefficient

$$C_f = \frac{2}{Re} \overline{\mu \frac{\partial u}{\partial z}}\bigg|_{z=0} ,$$

the decrease of the Stanton number

$$St = \frac{\bar{q}_W}{\bar{\rho}_W (T_W - T_\infty)}$$

and of the shape factor

$$H = \frac{\delta_1}{\delta_2}$$

(δ_2 is the compressible momentum thickness), are observed in the final stage of our simulation, figure 25. During linear and nonlinear stages these quantities remain close to their laminar values. The time at which C_f, St and H_{12} change dramatically coincides with the build-up of the primary shear-layer structures. Note that both the skin friction coefficient and the Stanton number overshoot the turbulent values (see Guo *et al.* 1994*a*). This behaviour is quite general to boundary-layer transition.

Temporal averages in the experiment correspond to streamwise (x) or plane (x, y) averages of the respective flow quantities in our computation. For a compressible flow Favre averages are preferable. Figure 26 shows a set of streamwise Favre-averaged

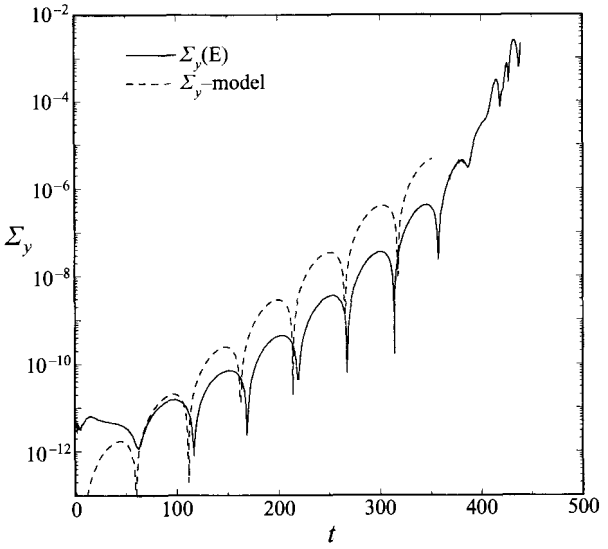

FIGURE 23. Temporal evolution of spanwise asymmetry, and comparison with a simplified model.

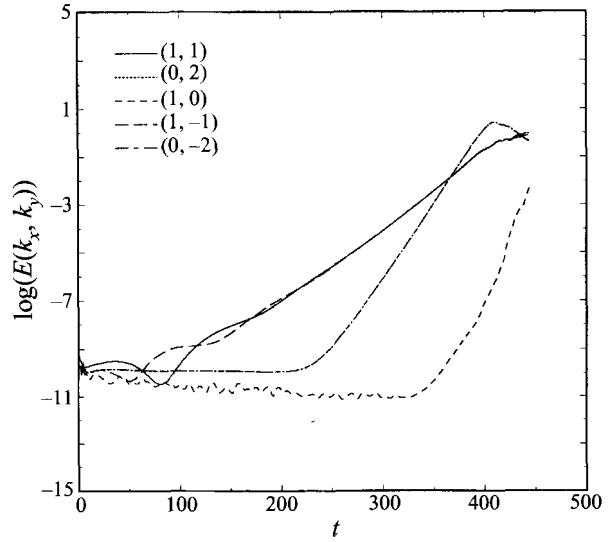

FIGURE 24. Mode energy evolution of spanwise-conjugate modes.

RMS-fluctuation distributions of the temperature. Initially the two-dimensional primary wave amplitude distribution is evident, figure 26(*a*). The secondary instability leads to a three-dimensional deformation near the critical layer, figure 26(*b*). The streamwise average over the full box length yields a double-peak structure near the critical layer typical of the subharmonic staggered Λ-vortex pattern. Along with the break-up of the Y-shear-layer the largest fluctuations can be observed, figure 26(*c*). The break-up of the upper shear layer causes a rapid spreading of fluctuations into the outer part of the boundary layer, figure 26(*d*).

Unfortunately there appear to be no experimental data available for the transition regime that could be compared with the present simulation results. However, Favre-averaged profiles of the final stage of the present simulation may be compared with

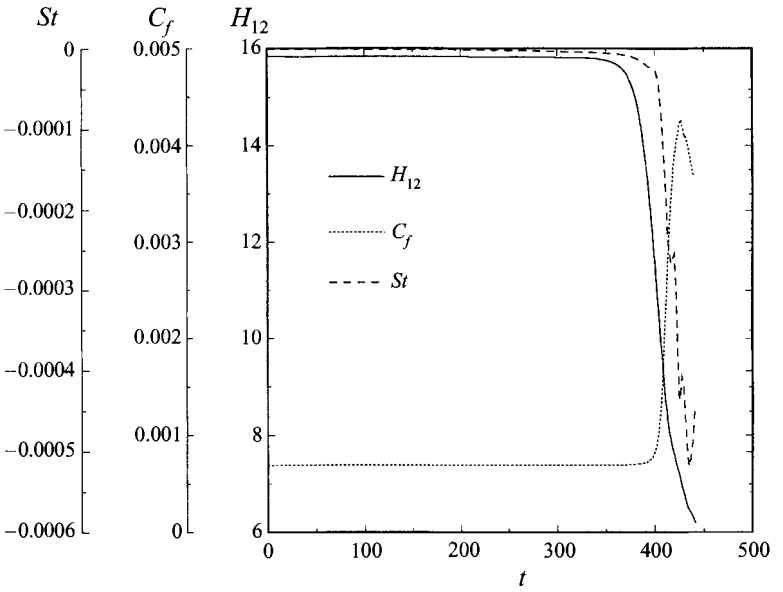

FIGURE 25. Temporal evolution of the shape factor H_{12}, the skin-friction coefficient C_f and the Stanton number St.

experimental results for a turbulent boundary layer, if M_∞ and T_∞ are comparable and T_W is not much different. This is the case for experiments by Mabey, Meier & Sawyer, documented in Fernholz & Finley (1977) (series 74021801), at $M_\infty = 4.52$, $Re_{\delta_1} = 89398$, $T_\infty^* = 61.81$ K, $T_W = 4.78$. The experimental wall temperature is larger than the adiabatic one. Starting from the laminar profiles, the transitional mean velocity and temperature profiles evolve towards the experimental results, figure 27(*a*) and figure 28(*a*). The distributions of the corresponding RMS-fluctuations, figures 27(*b*) and 28(*b*), still differ from expected turbulent profiles in that two local maxima of $(\overline{u'u'})^{1/2}$ and $(\overline{T'T'})^{1/2}$ are visible (see also Guo *et al.* 1995). The upper one is caused by the upper-shear-layer break-up and presumably disappears when this process is complete. The lower one is expected in a fully turbulent profile and indicates the onset of near-wall turbulence. The Reynolds stresses $\overline{\rho u'u'}$, figure 29(*a*), and $\overline{\rho u'w'}$, figure 29(*b*), and the Reynolds heat-flux $\overline{\rho w'T'}$, figure 30, show a similar behaviour. In particular, the spreading of the fluctuations from the critical layer is evident. It is interesting to note the sharp change of the RMS-profiles from the inner to the outer flow at the superlayer at about $z \simeq 3$ in the mean.

4. Discussion

The existence of a subharmonic temporal secondary instability is confirmed by the present numerical simulation. In agreement with the results of secondary instability theory the existence of a fundamental resonance can be excluded under the present conditions. The interpretation of experimental results by Stetson & Kimmel (1993) raises questions as to whether the subharmonic transition process is of significance in their experiments. Despite a clearly dominant second-mode primary instability no evidence for a subharmonic was found. Owing to a lack of three-dimensional data it unfortunately remains unclear how three-dimensional fluctuations are initiated, which are the necessary prerequisite to trigger laminar–turbulent breakdown. Candidates

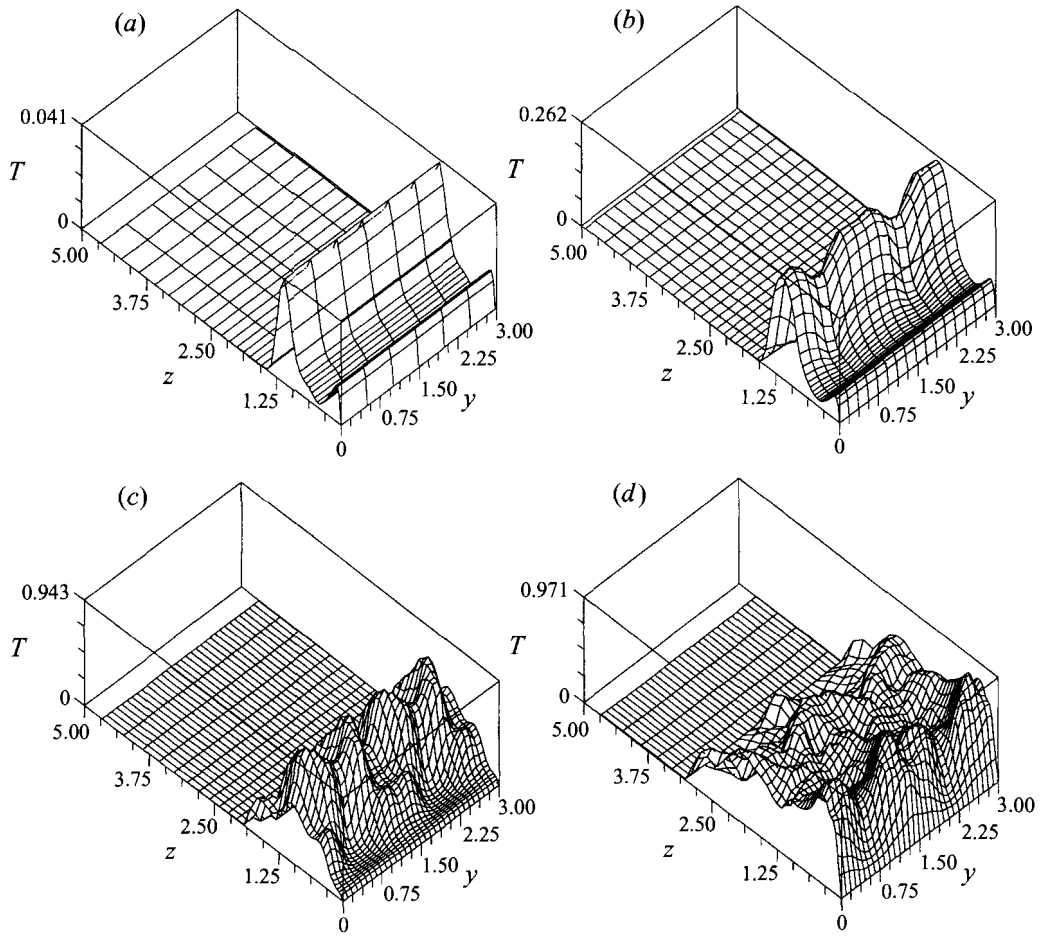

FIGURE 26. Carpet plots of the streamwise-averaged temperature fluctuations $(\overline{T'T'})^{1/2}$. (*a*) $t = 0$, (*b*) $t = 368.13$, (*c*) $t = 407.05$, (*d*) $t = 440.60$.

are the oblique-wave breakdown at high Mach number, where nonlinear interactions immediately follow the primary instability (oblique first-mode waves) (Adams 1993; Adams & Kleiser 1993*b*), and three-dimensional second-mode waves, as remarked by Stetson & Kimmel (1993), which are not the most unstable ones but may nevertheless be significantly amplified. The latter have recently been studied numerically by Pruett & Chang (1995).

Two characteristic primary vortex and shear-layer structures have been identified originating from the secondary wave. These appear in the staggered arrangement typical of the subharmonic type of transition. However, similar primary structures were also identified during the fundamental breakdown at the same flow parameters, though the further development appears to be different (Adams & Kleiser 1993*b*). At lower Mach numbers of about $M_\infty = 2$, Y-shaped shear layers have not been observed (Fasel *et al.* , 1993; Sandham *et al.* 1994).

The mechanism responsible for the shear-layer growth is supposed to resemble that of Stuart (1965), adapted to supersonic flow. Stuart's main conclusion is that the mean shear is redistributed by a pair of streamwise vortices and detached shear layers form due to convection and stretching of spanwise vorticity. With respect to a reference

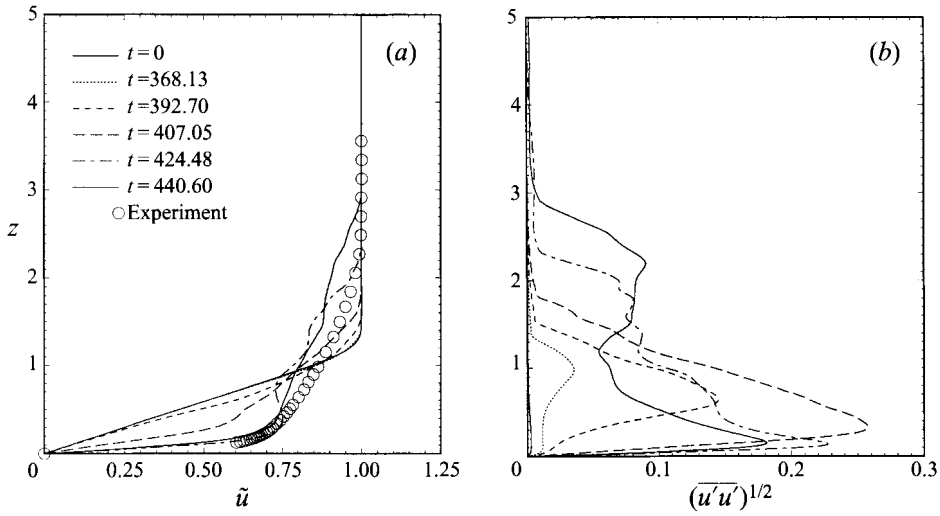

FIGURE 27. Mean velocity profile $\tilde{u}$ and RMS-fluctuations $(\overline{u'u'})^{1/2}$ at different times t. Symbols: turbulent profile, experiment 74021801 from Fernholz & Finley (1977). (*a*) $\tilde{u}$, (*b*) $(\overline{u'u'})^{1/2}$.

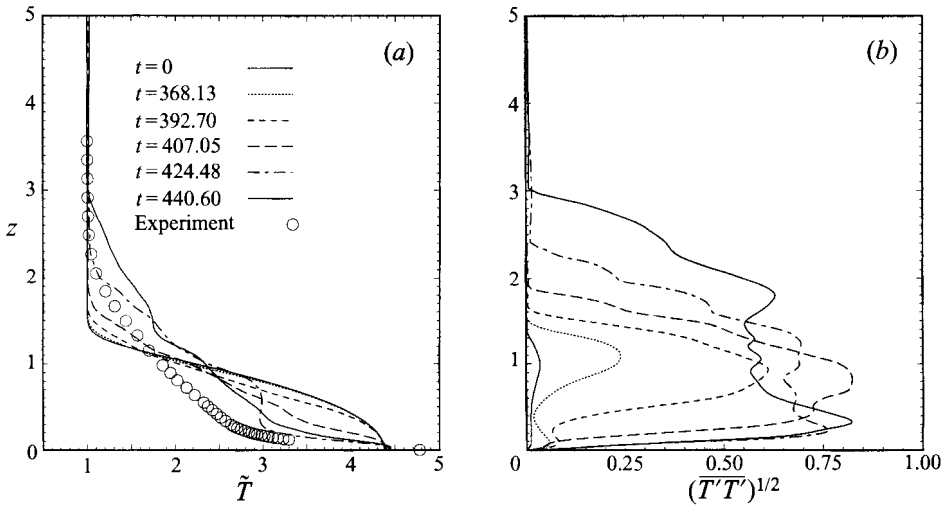

FIGURE 28. Mean temperature profile $\tilde{T}$ and RMS-fluctuations $(\overline{T'T'})^{1/2}$ at different times t. Symbols: turbulent profile, experiment 74021801 from Fernholz & Finley (1977). (*a*) $\tilde{T}$ (*b*) $(\overline{T'T'})^{1/2}$.

frame which moves downstream at about 90% of the free-stream velocity the flow can be separated into a near-wall relative-supersonic region and a relative-subsonic region above. Applying a Galileian transformation the flow becomes quasi-steady in a moving reference frame. The governing system of equations can be diagonalized along characteristic lines which are pointing solely upstream in the relative-supersonic part and both downstream and upstream in the relative-subsonic part. With respect to a linearized wave equation the quasi-steady flow is thus of hyperbolic type in the relative-supersonic part and of elliptic type in the relative subsonic part. Considering only a cross-plane (y, z), the whole region above the relative-sonic layer belongs to the region of influence of the streamwise vortices. However, the region between

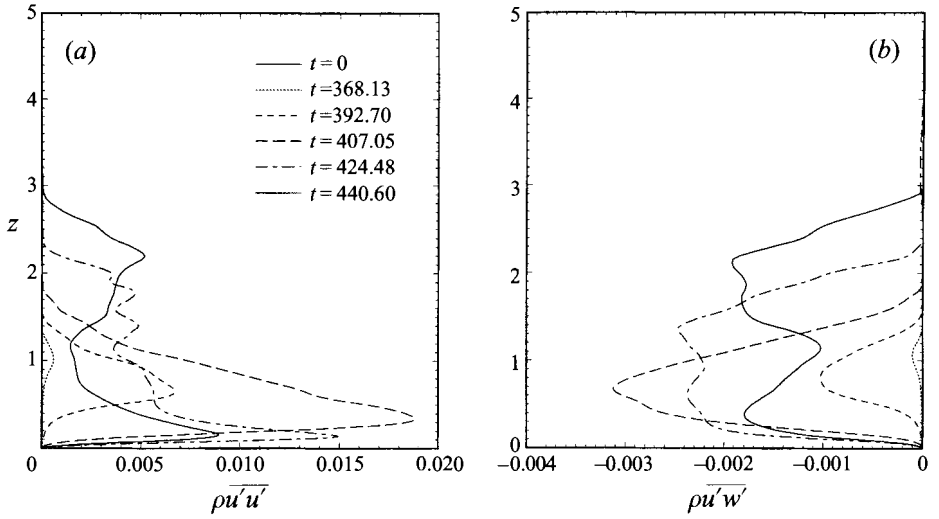

FIGURE 29. Reynolds stresses $\overline{\rho u'u'}$ and $\overline{\rho u'w'}$ at different times t. (*a*) $\overline{\rho u'u'}$, (*b*) $\overline{\rho u'w'}$.

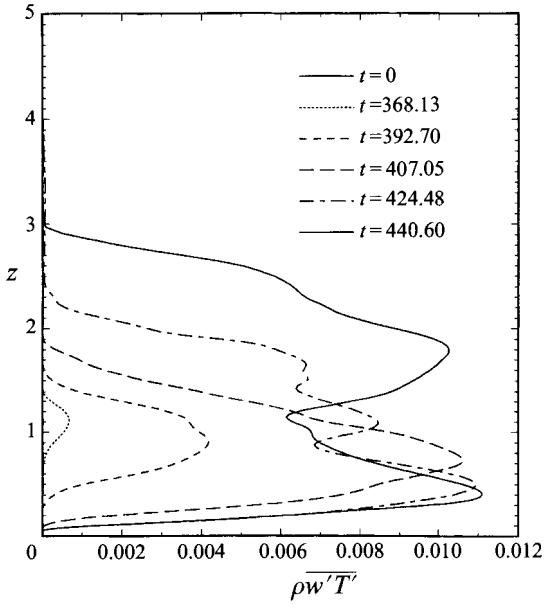

FIGURE 30. Reynolds heat-flux $\overline{\rho w'T'}$ at different times t.

the relative-sonic layer and the wall does not, and thus does not experience the cross-flow induced by the streamwise vortices. Thus in the relative-supersonic region the information about the cross-flow induced by the Stuart-vortex pair is convected downstream (with respect to the moving reference frame) along the characteristic curves and cannot build up a shear-layer structure in the cross-flow plane. In the relative-subsonic part, however, the influence of the cross-flow vortices accumulates and is responsible for the evolution of the observed shear layers.

It is interesting to note the dominance of streamwise-averaged modes during early breakdown, in particular the $(0, \pm 2)$-modes, which seems to be a feature almost inde-

pendent of the particular transition type. Once a pair of finite-amplitude oblique waves has evolved, modes with low streamwise wavenumbers are preferentially generated. An explanation of this behaviour has been suggested by Schmid & Henningson (1992) for incompressible channel flow. They point out that their findings may also be valid in more general cases. Pruett & Zang (1992) showed that the transition process can be inhibited by suppressing the $(0, \pm 2)$-modes artificially, although the fraction of total fluctuation energy of these modes is rather small. In the present simulation these modes reach their maximum energy content with the first shear-layer roll-up at about $t = 407$. At this time the spanwise fluctuation activity is maximum.

The general picture that emerges regarding shear-layer instability and break-up in the present $M_\infty = 4.5$ flow is the same as in Sandham & Kleiser (1992) for incompressible flow. They concluded that the instability and the break-up of the shear layers generated by the Λ-vortices are not a result of disturbance amplification from a stochastic background, but are deterministic and caused by large-amplitude perturbations at locations with are defined by the primary and secondary instability. The growth of the odd modes during the final stage of breakdown, explained in §3.1, indicates the 'onset of unpredictability' (Sandham & Kleiser 1992).

Owen & Horstmann (1972) report values of the convection velocities of organized structures in a turbulent boundary layer at $M_\infty = 7.2$ between $0.75U_\infty$ and $0.9U_\infty$. These velocities are comparable to those found from our data. Also, in the experiment as well as in our simulation the streamwise convection velocities are nearly independent of the size of the structures. Spina & Smits (1987) gave experimental results for the inclination angles of organized (presumably vortical) structures in a turbulent boundary layer at $M_\infty = 3$. These values have been found to agree well with the inclination of vortical structures at $t = 440.46$ of the present simulation, as noted in §3.4. An inclination close to the orientation of the mean shear rate yields the most effective way of energy conversion from the mean flow to fluctuations.

We believe that the mechanisms investigated herein are more generally valid as long as the primary instability wave travels with a low subsonic velocity with respect to the free stream. This is the case for second-mode waves, which become increasingly important with increasing Mach number. For lower Mach numbers (e.g. $M_\infty = 2$), where an oblique first-mode wave is the most unstable, there is a preference for more narrow streamwise vortices, and accordingly a different shear-layer structure evolves (e.g. Sandham *et al.* 1994). For an oblique mode transition at $M_\infty = 4.5$ with a first mode as fundamental wave, a primary vortex and shear-layer structure similar to that in the subharmonic type of transition can be observed (Adams & Kleiser 1993*b*). A wider spanwise spacing and a stronger streamwise alignment may be responsible for the fact that no upper shear layer can be observed in this case. Depending on the Reynolds number and the disturbance excitation, at $M_\infty = 4.5$ either the first- or the second-mode wave can be dominant, thus this might be a borderline case. Within a temporal instability model not taking into account the spatial growth of the laminar boundary layer, a prediction of the most likely transition mechanism is difficult. Recent temporal simulation results by Guo *et al.* (1995, 1996) show that by taking into account certain terms associated with the growth of the laminar boundary layer within a moving reference frame, spatial simulation results can be closely reproduced during the linear and early nonlinear stages. We emphasize that the particular transition process is selected during the primary linear instability evolution. Once it is selected, the subsequent nonlinear breakdown is believed to be captured accurately by a temporal simulation.

5. Conclusions

In summary, the transition process in a $M_\infty = 4.5$ flat-plate boundary layer was investigated by direct simulation using the temporal approach. Initially a two-dimensional second-mode primary-wave disturbance, which moves downstream with a phase speed close to the free-stream velocity, plus small random noise was superimposed on the laminar basic flow. It was found that a subharmonic secondary instability mode emerges from the background noise, in accordance with secondary stability theory.

The subsequent nonlinear stages of the transition process have been analysed in detail up to the beginning of turbulence, and can be described as follows. The three-dimensional subharmonic instability deforms the primary vortices near the critical layer into a system of staggered Λ-vortices. This happens in the relative subsonic part of the boundary layer. The cross-flow motion induced by the Λ-vortices generates two types of shear layers. The first one, below the Λ-vortices and above the relative sonic layer, is Y-shaped and dominates the first phase of breakdown. The second one, which is located above the laminar boundary layer edge, behaves similarly to the 'high-shear layer' well-known from incompressible transition, is mainly restricted to a peak plane, and dominates the second phase of break-down. The break-up of the Y-shaped shear layer generates vortices below and above the critical layer, which split the former Λ-vortices into successively smaller parts. A common feature of these events is that they mostly appear near the centre of the remnants of the Λ-vortex legs, where these are torn off. Although they form (looking from above) Λ-like or inverse-Λ-like patterns, their general shape is quite different and has not been observed in lower Mach number flow so far. The shear-layer formation takes place in the relative subsonic part of the boundary layer and can be explained by the Stuart mechanism, adapted to compressible flow.

The break-up of the upper-shear-layer takes place when the Y-shaped shear layer has gone through its break-up stages. It shows phenomena quite similar to those well-known from incompressible boundary layer transition, such as arch- and barrel-shaped vortices which evolve into hairpin vortices and vortex loops. The break-up of the Y-shaped shear layer is mainly confined to the off-peak planes while the upper-shear-layer break-up mainly happens at peak planes. The perturbation then spreads between the peak and off-peak planes due to an interaction of the vortical structures emerging from both events.

The spanwise asymmetry which is seeded by the initial noise spectrum was found to grow throughout the linear and weakly nonlinear stages along with the subharmonic waves. The onset of a rapid growth of modes with an odd sum k_x+k_y of wavenumbers coincides with a more pronounced increase of spanwise asymmetry, indicating the onset of unpredictability in the flow. The different phases of shear-layer break-up are reflected in the evolution of averaged quantities. Mean velocity and temperature profiles evolve towards experimentally measured turbulent profiles.

We would like to mention the fruitful cooperation with Dr N. D. Sandham, now at Queen Mary and Westfield College, London, during the earlier stage of this work. We are indebted to him for numerous helpful discussions and for valuable comments on a draft version of this paper. Dr C. D. Pruett (NASA LaRC) kindly provided secondary instability data. For the three-dimensional visualizations the graphics package COMADI by H. Vollmers (DLR) was used. The final part of the numerical simulation presented was made possible by a CPU-time grant of CRAY Research, Germany. We are grateful to Dr W. Oed (CRAY) for his assistance.

REFERENCES

ADAMS, N. A. 1993 Numerische Simulation von Transitionsmechanismen in kompressiblen Grenzschichten. Doctoral Thesis, Technische Universität München; also *DLR-FB* 93-29, DLR, Germany (in German).

ADAMS, N. A. & KLEISER, L. 1993*a* Numerical simulation of transition in a compressible flat plate boundary layer. In *Transitional and Turbulent Compressible Flows* (ed. L. D. Kral & T. A. Zang). ASME-FED vol. 151, pp. 101–110.

ADAMS, N. A. & KLEISER, L. 1993*b* Numerical simulation of fundamental breakdown of a laminar boundary-layer at Mach 4.5. *AIAA Paper* 93-5027.

ADAMS, N. A., SANDHAM, N. D. & KLEISER, L. 1992 A method for direct numerical simulation of compressible boundary-layer transition. In *Notes on Numerical Fluid Mechanics*, vol. 35 (ed. J. B. Vos, A. Rizzi & I. Rhyming), pp. 523–532. Vieweg.

CANUTO, C., HUSSAINI, M. Y., QUARTERONI, A. & ZANG, T. A. 1988 *Spectral Methods in Fluid Dynamics*. Springer.

CARPENTER, M. H., GOTTLIEB, D. & ABARBANEL, S. 1993 The stability of numerical boundary treatments for compact high-order finite difference schemes. *J. Comput. Phys.* **108**, 272–295.

DRAZIN, P. G., REID W. H. 1981 *Hydrodynamic Stability*. Cambridge University Press.

EISSLER, W. & BESTEK, H. 1993 Spatial numerical simulations of nonlinear transition phenomena in supersonic boundary layers. In *Transitional and Turbulent Compressible Flows* (ed. L. D. Kral & T. A. Zang) 101–110. ASME-FED vol. 151, pp. 69–76.

ERLEBACHER,G. & HUSSAINI, M. Y. 1990 Numerical experiments in supersonic boundary-layer stability. *Phys. Fluids* A **2**, 94–104.

FASEL, H., THUMM, A. & BESTEK, H. 1993 Direct numerical simulation of transition in supersonic boundary layers: oblique breakdown. In *Transitional and Turbulent Compressible Flows* (ed. L. D. Kral & T. A. Zang). ASME-FED vol. 151, pp. 77–92.

FERNHOLZ, H. H. & FINLEY, P. J. 1977 A critical compilation of compressible boundary layer data with a survey of turbulent data. *AGARDograph* 263.

GUO, Y., ADAMS, N. A., KLEISER, L. 1995 Modeling of nonparallel effects in temporal direct numerical simulations of compressible boundary layer transition. *Theor. Comput. Fluid Dyn.* 7, 141–157.

GUO, Y., ADAMS, N. A., SANDHAM, N. D. & KLEISER, L. 1994 Numerical simulation of supersonic boundary layer transition. *AGARD* CP-551.

GUO, Y., KLEISER, L. & ADAMS, N. A. 1996 A comparison study of an improved temporal DNS and spatial DNS of compressible boundary layer transition. *AIAA J.* **34** (in press).

HERBERT, T. 1988 Secondary instability of boundary layers. *Ann. Rev. Fluid Mech.* **20**, 487–526.

KACHANOV, Y. S. & LEVCHENKO V. Y. 1984 The resonant interaction of disturbances at laminar-turbulent transition in a boundary layer. *J. Fluid Mech.* **138**, 209–247.

KENDALL, J. M. 1967 Supersonic boundary layer stability experiments. In *Boundary Layer Transition Study Group Meeting, Vol. II*, BSD-TR-67-213, USAF (ed. W. D. McCauley), pp. 10-1–10-8.

KOSINOV, A. D., MASLOV, A. A. & SHEVELKOV, S. G. 1990 Experiments on the stability of supersonic laminar boundary layers. *J. Fluid Mech.* **219**, 621–633.

LELE, S. K. 1992 Compact finite difference schemes with spectral-like resolution. *J. Comput. Phys.* **103**, 16–42.

MACK, L. M. 1984 Boundary-layer linear stability theory. In *Special Course on Stability and Transition of Laminar Flow, AGARD Rep.* 709, pp. 3-1–3-81.

MACK, L. M. 1990 On the inviscid acoustic-mode instability of supersonic shear flows. Part 1. Two-dimensional waves. *Theor. Comp. Fluid Dyn.* **2**, 97–123.

MAYER, E. W. & POWELL, K. G. 1992 Similarity solutions for viscous vortex cores. *J. Fluid Mech.* **238**, 487–507.

MOIN, P., LEONARD, A. & KIM, J. 1986 Evolution of a curved vortex filament into a vortex ring. *Phys. Fluids* **29**, 955–963.

NG, L. & ERLEBACHER, G. 1992 Secondary instabilities in compressible boundary layers. *Phys. Fluids* A **4**, 710–726.

OWEN, F. K. & HORSTMAN, C. C. 1972 On the structure of hypersonic turbulent boundary layers. *J. Fluid Mech.* **53**, 611–636.

PRUETT, C. D. & CHANG, C. L. 1993 A comparison of PSE and DNS for high-speed boundary-layer flows. In *Transitional and Turbulent Compressible Flows*, (ed. L. D. Kral & T. A. Zang). ASME-FED vol. 151, pp. 57–67.

PRUETT, C. D. & CHANG, C.-L. 1995 Spatial direct numerical simulation of high-speed boundary-layer flows — part II: transition on a cone in Mach 8 flow. *Theor. Comp. Fluid Dyn.* **7**, 397–424.

PRUETT, C. D. & ZANG, T. A. 1992 Direct numerical simulation of laminar breakdown in high-speed, axisymmetric boundary layers. *Theor. Comp. Fluid Dyn.* **3**, 345–367.

PRUETT, C. D., ZANG, T. A., CHANG, C.-L. & CARPENTER, M. H. 1995 Spatial direct numerical simulation of high-speed boundary-layer flows — part I: algorithmic considerations and validation. *Theor. Comp. Fluid Dyn.* **7**, 49–76.

SANDHAM, N. D., ADAMS, N. A. & KLEISER, L. 1994 Direct simulation of breakdown to turbulence following oblique instability waves in a supersonic boundary layer. In *Direct and Large-Eddy Simulation I* (ed. P. R. Voke *et al.*), pp. 213–223.

SANDHAM, N. D. & KLEISER, L. 1992 The late stages of transition to turbulence in channel flow. *J. Fluid Mech.* **245**, 319–348.

SANDHAM, N. D. & REYNOLDS, W. C. 1991 Three-dimensional simulations of large eddies in the compressible mixing layer. *J. Fluid Mech.* **224**, 133–158.

SARKAR, S., ERLEBACHER, G., HUSSAINI, M. Y. & KREISS, H. O. 1991 The analysis and modeling of dilatational terms in compressible turbulence. *J. Fluid Mech.* **182**, 85–109.

SCHMID, P. J. & HENNINGSON, D. S. 1992 A new mechanism for rapid transition involving a pair of oblique waves. *Phys. Fluids A* **4**, 1986–1989.

SIMEN, M. & DALLMANN, U. 1992 On the instability of hypersonic flow past a pointed cone – comparison of theoretical and experimental results at Mach 8. *DLR FB* 92-02, DLR, Germany.

SPALART, P. R. & YANG, K. S. 1987 Numerical study of ribbon-introduced transition in Blasius flow. *J. Fluid Mech.* **178**, 345–365.

SPINA, E. F. & SMITS, A. J. 1987 Organized structures in a compressible turbulent boundary layer. *J. Fluid Mech.* **227**, 473–493.

STETSON, K. F. & KIMMEL, R. L. 1992 On hypersonic boundary layer stability. *AIAA Paper* 92-0737.

STETSON, K. F. & KIMMEL, R. L. 1993 On the breakdown of a hypersonic laminar boundary layer. *AIAA Paper* 93-0896.

STEWARTSON, K. 1964 *The Theory of Laminar Boundary Layers in Compressible Fluids*. Oxford University Press.

STUART, J.T. 1965 The production of intense shear layers by vortex stretching and convection. *AGARD Rep.* 514.

THOMPSON, K.W. 1987 Time dependent boundary conditions for hyperbolic systems. *J. Comput. Phys.* **68**, 1–24.

THUMM, A., WOLZ, W. & FASEL, H. 1990 Numerical simulation of spatially growing three-dimensional disturbance waves in compressible boundary layers. In *Laminar-Turbulent Transition* (ed. D. Arnal & R. Michel), 303–308, Springer.

VOLLMERS, H., KREPLIN, H.-P. & MEIER H.U. 1983 Separation and vortical-type flow around a prolate spheroid – evaluation of relevant parameters. *AGARD CP* 342, pp. 14-1–14-14.

WRAY, A.A. 1986 Very low storage time-advancement schemes. *Internal Rep.* NASA Ames Research Center, Moffet Field, California.

ZEMAN, O. 1990 Dilatation dissipation: The concept and application in modeling compressible mixing layers. *Phys. Fluids* A **2**, 178–188.